Analytical and Computational Micromechanics Analysis of the Effects of Interphase Regions, Bundling, and Orientation on the Effective Coefficient of Thermal Expansion of Carbon Nanotube-Polymer Nanocomposites

Skylar N. Stephens

Thesis submitted to the Faculty of the

Virginia Polytechnic Institute and State University

in partial fulfillment of the requirements for the degree of

Master of Science

in

Ocean Engineering

Gary D. Seidel, Chair

Alan J. Brown

Owen F. Hughes

May 08, 2013

Blacksburg, Virginia

Keywords: multiscale, carbon nanotube , thermal expansion, interphase, bundling, orientation, micromechanics

Analytical and Computational Micromechanics Analysis of the Effects of Interphase Regions, Bundling, and Orientation on the Effective Coefficient of Thermal Expansion of Carbon Nanotube-Polymer Nanocomposites

Skylar N. Stephens

(ABSTRACT)

Analytic and computational micromechanics techniques based on the composite cylinders method and the finite element method, respectively, have been used to determine the effective coefficient of thermal expansion (CTE) of carbon nanotube-epoxy nanocomposites containing aligned nanotubes. Both techniques have been used in a parametric study of the influence of interphase stiffness and interphase CTE on the effective CTE of the nanocomposites. For both the axial and transverse CTE of aligned nanotube nanocomposites with and without interphase regions, the computational and analytic micromechanics techniques were shown to give similar results. The Mori-Tanka method has been used to account for the effect of randomly oriented fibers. Analytic and computational micromechanics techniques have also been used to assess the effects of clustering and clustering with interphase on the effective CTE components. Clustering is observed to have a minimal impact on the effective axial CTE of the nanocomposite and a 3-10%. However, there is a combined effect with clustering and one of the interphase layers.

This work received support from the Science, Mathematics and Research for Transformation (SMART) Scholarship.

Acknowledgments

I would like to first thank my advisor, Dr. Gary Seidel, for his tremendous support and encouragement. I am very fortunate that Dr. Seidel offered me a chance to complete undergraduate research as this opportunity opened my eyes to the world of graduate school. His professional and academic guidance have opened up many doors for me, and for that I express my gratitude. His enthusiasm to learn and to teach is inspiring as I try to model my academic and professional career after his. I am very grateful for the opportunity to learn from Dr. Seidel, and I look forward to continuing my professional growth under his guidance.

I would like to thank my other committee members, Dr. Alan Brown and Dr. Owen Hughes. Their critiques will certainly help to improve upon the final form of this thesis. Both Dr. Brown and Dr. Hughes inspired me immensely in the classroom as an undergrad to continue my studies in Ocean Engineering. I have learned a great deal from Dr. Brown and Dr. Hughes, and I see both as role models for my academic career.

I would also like to thank the American Society for Engineering Education (ASEE) and the Science, Mathematics and Research for Transformation (SMART) Scholarship. The scholarship for service program has provided me with the great opportunity to further my education and to secure a job with the DoD, something I consider to be a patriotic privilege.

I am also indebted to Dr. Judy Conley of the Naval Surface Warfare Center Carderock Divison (NSWCCD). I am grateful that she saw potential in my research and selected me for the SMART Scholarship. Her professional guidance and support are appreciated, and I look forward to our continued professional relationship.

Last, I would like to thank my parents, Karen and Wesley Stephens. Their love and support throughout my Master's work has been unwavering and very much cherished. Thank you for instilling a love of learning in me at a very young age and for nurturing my curiosity. I owe much of my success, both personally and professionally, to their constant positive influence.

Contents

List of Figures

List of Tables

1 Introduction

The incentive for advanced composite research is mounting, and is being driven by the U.S defense industry as well as the commercial sector. In the continuing process of increasing performance and reducing cost, military and commercial aircraft and ship design faces a number of challenges. Among these are challenges associated with fatigue life, electrostatic discharge, and thermal management. These challenges are increasingly being dealt with by relying on composite materials, as opposed to the more traditional metallic materials. The use of these materials in the construction of aerospace and marine vehicles offers the potential to enhance mechanical, electrical, and thermal properties. With all of this potential, it is clear that the use of composite materials will continue to grow, and grow rapidly. Nanocomposites are one such composite material. Reliable and thorough quantification of nanocomposite properties is a prerequisite to the effective use of these materials. The current research is intended to contribute to the growing body of knowledge concerning nanocomposite properties, specifically effective thermal expansion coefficients.

Composite materials are currently being used in order to arrest crack propagation and to fix damage on ships through the use of composite patches [1]. A schematic of this patch on a ship deck can be seen in Figure 1. Finalized composite patches on a ship can be seen in Figure 2. Nanocomposite materials offer the potential for structural health monitoring (SHM) in the patch and in other ocean structures through a thorough quantification of the piezoresistive effect. SHM has the potential to lead to reduced ship maintenance and operating costs. Thermal expansion activates a piezoresistive sensor, and this thermal response must be separated from other sensor data. It is therefore necessary to calibrate a structural health monitoring sensor based on ambient environmental temperature. This research also offers the potential for developing structural health monitoring sensor materials that address maritime issues associated with nominal mechanical, thermal, and environmental load cycles (e.g. fatigue, cavitation, and corrosion) and inadvertent overload events (e.g. docking accidents and battle damage) in order to transition to a cost reducing condition based maintenance program. This would require developing a prototype carbon-nanotube elastomer nanocomposite with tailored piezoresistive response for structural health monitoring sensors. It would also require the

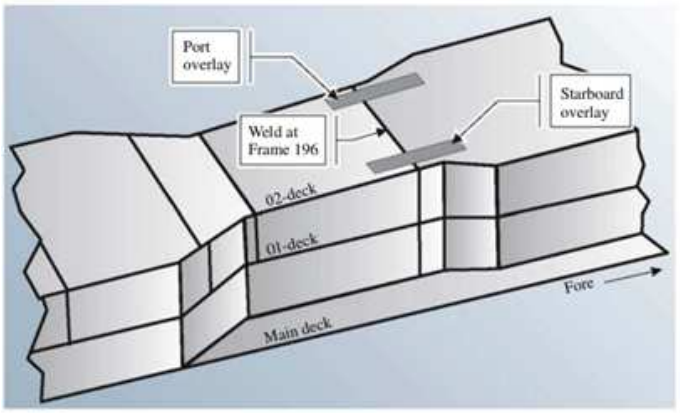

Figure 1: Composite patch located on ship deck from Ref. [1] Grabovac, I. and Whittaker, D., "Applications of bonded composites in the repair of ships structures - A 15-year service experience," *Elsevier Composites: Part A*, 2009. Used under fair use, 2013.

characterization of the the response of the piezoresistive nanocomposite as a structural health monitoring sensor. Work is currently being done to create a multiscale model for the coupled mechanical-electrical response of the piezoresistive nanocomposite material as a function of nanotube concentration, orientation and distribution [3, 7]. Future work will introduce damage models associated with maritime applications and environments into the multiscale model in order to tailor the structural health monitoring system for naval systems.

The piezoresistive phenomenon is the change in electrical resistivity due to a deformation (coupled mechanical-electrical response). Some monolithic materials exhibit changes in their effective electrical conductivities, and thus electrical resistivities, in the presence of a deformation. For example, the piezoresistive phenomenon has been described in silicon materials by use of many-valley energy surfaces [8]. These valleys all have an equal number of electrons in them when the material is in the reference configuration, and the silicon material therefore has isotropic electrical conductivity. An applied uniaxial extension deforms the body and therefore also changes its geometry. This deformation does not change the amount of conduction electrons, but it does cause there to be a higher electron density along the axis of applied strain. Electrons will therefore

(a) Composite patch in machinery room.

(b) Composite patch on deck.

Figure 2: Composite patches installed on a ship from Ref. [2] Bartlett, S. and Jones, B., "Composite Ship Structures," *ASNE Day 2013: Engineering America's Maritime Dominance*, ASNE, Arlington, Virginia, February 21-22 2013. Used under fair use, 2013.

have a larger mobility along the axis of applied strain. The resistivity will thus decrease as the conductivity increases in the presence of an applied electric field along the same axis. The silicon material therefore has a strain-induced or deformation induced electrical conductivity.

The literature has shown the presence of the piezoresistive phenomenon in single-walled carbon nanotubes. Tombler [9] showed experimentally the potential to use strain to tune the band gap of nanotubes and thus the electrical resistivity. This work showed that high strains can lead to large changes in the conducting capabilities of the nanotubes. In this sense, the SWCNTs are similar to silicon materials in that each exhibits inherent piezoresistivity.

The nanoscale effect of electron hopping in nanotube-polymer nanocomposites has been described as a mechanism of electron transfer between carbon nanotubes [8]. Electron hopping in a nanoscale RVE for carbon nanotubes is modeled by use of an electrically conductive interphase layer that exists between the carbon nanotubes and the polymer matrix. Percolation of the electrical conductivity is shown to occur when the volume fraction of carbon nanotubes dispersed in a polymer matrix increases to the point at which

the interphase layers of the adjacent nanotubes come into contact. The nanotube-polymer nanocomposite transitions from a three-phase to a two-phase material as the volume fraction of nanotubes is increased. This increasing volume fraction eventually leads to a fully percolated material as all residual polymer matrix material is lost and the nanotubes are only separated by the interphase material. There is an increase in electrical conductivity at this percolation volume fraction because the conductive interphase layers have now come into contact [10].

It follows that a structural piezoresistive response could also be seen in nanotube-polymer nanocomposites [3]. The geometry of the nanocomposite could be changed due to an applied uniaxial deformation, an increase in nanotube volume fraction, or clustering and interphase effects. A large enough deformation or an increase in nanotube volume fraction could cause a visible impact on the effective electrical conductivity as the nanotubes would be closer to coming into contact with each other. This idea is similar to the electron hopping phenomenon in that both describe effective properties as functions of structural elements.

A composite material where one or more of the constituent phases has a length on the order of nanometers is considered to be a nanocomposite. The work described herein focuses on single-wall carbon nanotubes (SWCNT) as the nano length reinforcing element. SWCNTS are sheets of graphene that have been rolled into the shape of a tube [4].

Nanocomposites offer the potential to address mechanical, thermal, and electrical issues simultaneously, and are thus termed a multifunctional material. The interest in developing multifunctional materials for use in advanced structures in the aerospace and naval industries has been one of the contributing factors encouraging the development of nanocomposites. In particular, nanocomposites consisting of single-wall carbon nanotubes (SWCNTs) dispersed in a polymer matrix have been proposed by many as a material capable of providing enhanced elastic, thermal and electrical properties relative to the neat polymer matrix materials typically used in traditional structural carbon fiber composites [11, 12, 13, 14]. The intent is to allow for the development of carbon fiber composites which can serve not only as a key structural element, but which are capable of providing improved thermal management, electrostatic static discharge, and structural health

monitoring abilities with negligible increases in weight [14, 15, 16]. As a result of the orders of magnitude difference in properties between SWCNTs and most polymers [1], it is believed that only a small amount of SWCNTs would be needed to impart large increases in the elastic, thermal and electrical properties. Recent characterization efforts have shown this to certainly be the case for the electrical properties of nanocomposites where fractions of a weight percent of SWCNTs have been shown to lead to percolation and a corresponding six to eight orders of magnitude increases in electrical conductivity relative to that of the neat polymer [20, 21, 22, 23, 24, 25]. Relatively large increases of 20 - 30% and 30-100% have also been observed in elastic properties [26, 27, 28] and thermal conductivities [29, 30, 31], respectively, of nanocomposites containing on the order of 1% SWCNTs, thereby confirming the potential of nanocomposites as multifunctional matrix materials for use in structural carbon fiber composites.

In an effort to explore the design space for multifunctional nanocomposite materials, there has been a significant amount of research devoted to developing multiscale models for carbon nanotube-polymer nanocomposites[32, 33]. Some of our recent work in this area has focused on the development of both analytic and computational micromechanics models[5, 34, 35, 10, 36, 37, 38] for assessing the effects of interphase regions, clustering, orientation, distribution, and nanoscale effects such as interfacial thermal resistance[35] and electron hopping[10] on the effective elastic properties and thermal and electrical conductivities of carbon nanotube-polymer nanocomposites; making use of input from lower length scale molecular dynamics simulations when possible. In particular, our efforts to model the thermal conductivity of nanocomposites have made use of molecular dynamics simulations for the measurement of the nanoscale effect associated with an interfacial thermal resistance between the nanotube and the surrounding polymer. This effect has been incorporated into both analytic and computational micromechanics approaches as a zero-thickness interface layer in the calculation of the effective thermal conductivity of nanocomposites containing randomly oriented carbon nanotubes, the results of which have compared favorably with nanocomposite characterization efforts. While these models provide a design tool for the primary variable regarding the use of nanocomposites in ther-

[1] Young's modulus, thermal conductivity and electrical conductivity of SWCNTs can be as much as 3, 4, and 14 orders of magnitude, respectively, larger than typical values reported for neat epoxy [17, 18, 19]

mal management applications in structural composites, also of significant interest, particularly in terms of thermal cycling and its effects on service life estimates, is controlling the mismatch in coefficient of thermal expansion between the structural fibers and the surrounding matrix. As such, the present work is focused on developing a multiscale model for determining the effective coefficient of thermal expansion in carbon nanotube-polymer nanocomposites for incorporation with the thermal conductivity model developed, and thereby allowing for improved design of nanocomposites for thermal management applications.

In the present work, analytic and computational micromechanics techniques are applied towards predicting the effective coefficients of thermal expansion of polymer nanocomposites containing aligned and randomly oriented bundles of SWCNTs [39]. For well-dispersed SWCNTs, plane strain composite cylinders analytic micromechanics approaches are applied for determining the coefficients of thermal expansion for aligned nanotube cases. In computational micromechanics approaches, periodic arrangements of well-dispersed SWCNTs are studied using the commercially available finite element software COMSOL Multiphysics 3.4. Periodic boundary conditions corresponding to axial and transverse constrained uniform temperature increase are applied to determine the corresponding local stress distribution within a given representative volume element (RVE), and subsequently, the components of the concentration tensors. RVEs are constructed with either hollow CNTs (in what would be termed a single step method), or using effective solid nanotubes having transversely isotropic effective properties determined from a composite cylinder approach (i.e., a two-step method), and are observed to yield nearly identical results for effective bundle coefficient of thermal expansion. The influence of the presence of an interphase region on the effective coefficient of thermal expansion is considered in a parametric study in terms of both interphase thickness, elastic properties, and coefficient of thermal expansion. Special emphasis is placed on assessing the impact of interphase percolation on the effective coefficient of thermal expansion. The resulting changes in effective coefficient of thermal expansion due to the presence of interphase regions are then put into context by comparison with an analogous parametric study on the effects of interphase regions on the effective elastic properties and thermal and electrical conductivities of nanocomposites. The thesis work also presents analytical and computational models to

assess the effect of nanotube bundling and bundling with interphase on the effective coefficients of thermal expansion using the same parametric study.

Micromechanics research for effective mechanical properties ([34]), effective electrical properties ([20, 23, 37]), and effective thermal conductivities ([31, 35]) has been conducted. However, micromechanics research has not been conducted on effective CTE. This thesis work will model effective CTE for an epoxy nanocomposite material system, and it will put into the context of a structural health monitoring sensor for composite patch applications on ships.

2 Description of Micromechanics Models

The multiscale modeling idealization for nanocomposites consisting of aligned and randomly oriented bundles of SWCNTs dispersed in a polymer matrix is shown schematically in Figure 3.

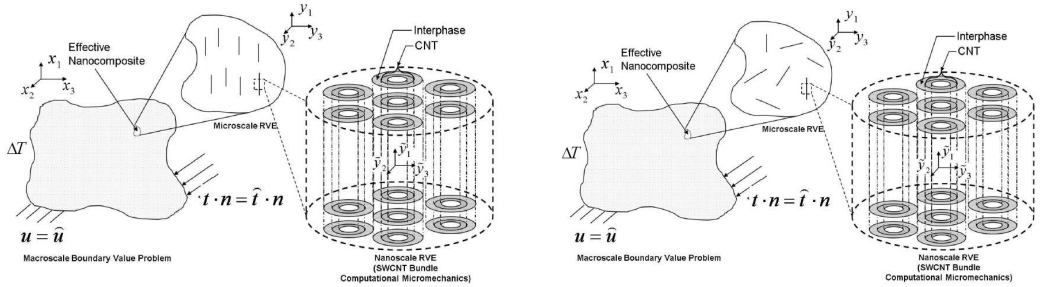

(a) Aligned

(b) Randomly Oriented

Figure 3: Hierarchical multiscale modeling idealization for nanocomposites comprised of aligned and randomly oriented bundles of SWCNTs dispersed in a polymer matrix.

This macroscale boundary value problem shows that microscale details, such as the alignment of the SWCNT bundles, can affect macroscale properties. It also shows that nanoscale details, such as the addition of an interphase layer to capture the nanoscale effects of polymer structure perturbation or the degree of SWCNT bundling, can affect microscale properties. For a given set of boundary conditions at the macroscale, the macroscale stress, $\boldsymbol{\sigma}$, can be determined from the static equilibrium equations which can be expressed in vector-tensor notation as:

$$\nabla \cdot \boldsymbol{\sigma} + \mathbf{f} = \mathbf{0} \tag{2.1}$$

where $\mathbf{f}$ is the macroscale body force and the del operator (∇) is applied with respect to the macroscale coordinate system (x_i). The macroscale infinitesimal total strain, ${}^{\mathrm{Tot}}\boldsymbol{\epsilon}$, is expressed in terms of the macroscale displacement, $\mathbf{u}$, by

$${}^{\mathrm{Tot}}\boldsymbol{\epsilon} = \frac{1}{2}\left(\nabla\mathbf{u} + (\nabla\mathbf{u})^{\mathrm{T}}\right) \tag{2.2}$$

where the superscript T denotes the transpose of the displacement gradient. The macroscale infinitesimal

total strain can be decomposed into two parts, the macroscale infinitesimal elastic strain, ${}^{\mathrm{El}}\boldsymbol{\epsilon}$, and the thermal strain, ${}^{\mathrm{T}}\boldsymbol{\epsilon}$, i.e.

$$ {}^{\mathrm{Tot}}\boldsymbol{\epsilon} = {}^{\mathrm{El}}\boldsymbol{\epsilon} + {}^{\mathrm{T}}\boldsymbol{\epsilon} \tag{2.3} $$

where the thermal strain can be expressed in terms of the temperature change between the current and reference configurations as

$$ {}^{\mathrm{T}}\boldsymbol{\epsilon} = \boldsymbol{\alpha}^{\mathrm{eff}}\Delta T = \boldsymbol{\alpha}^{\mathrm{eff}}(T - T_0) \tag{2.4} $$

with T and T_0 denoting the temperature in the current and reference configurations, respectively. The macroscale stress is related to the macroscale infinitesimal elastic strain through the linear elastic constitutive relation expressed as:

$$ \boldsymbol{\sigma} = \mathbf{L}^{\mathrm{eff}\,\mathrm{El}}\boldsymbol{\epsilon} \tag{2.5} $$

The tensors $\boldsymbol{\alpha}^{\mathrm{eff}}$ and $\mathbf{L}^{\mathrm{eff}}$ in Eqns 2.4 and 2.5 are the effective coefficient of thermal expansion and effective elastic stiffness for the nanocomposite, respectively, both of which are determined from the microscale representative volume element (RVE) with input obtained from the nanoscale RVE. Thus, the macroscale thermoelastic constitutive relationship can be expressed in terms of both the effective coefficient of thermal expansion and effective stiffness as

$$ \boldsymbol{\sigma} = \mathbf{L}^{\mathrm{eff}}\left({}^{\mathrm{Tot}}\boldsymbol{\epsilon} - \boldsymbol{\alpha}^{\mathrm{eff}}\Delta T\right) \tag{2.6} $$

so that the focus is therefore on determining effective properties by studying the micro- and nanoscale RVEs.

2.1 Composite Cylinders Method (CCM) for Effective Coefficient of Thermal Expansion

A composite cylinders approach, originally proposed by Hashin and Rosen [40], is used to analytically calculate effective CTE for the nanocomposite. The CCM model is beneficial because it allows for analytic modeling of hollow fibers, and interphase layers are easily as an additional layer in the composite cylinder assemblage. However, the CCM can only model one type of fiber at a time with at most transversely

isotropic material symmetry. The composite cylinders method realizes the nanoscale RVE as a concentric set of cylinders, the composite cylinder assemblage, which in the context of this thesis consists of a hollow CNT, an interphase region, and the polymer matrix as seen in Figure 4.

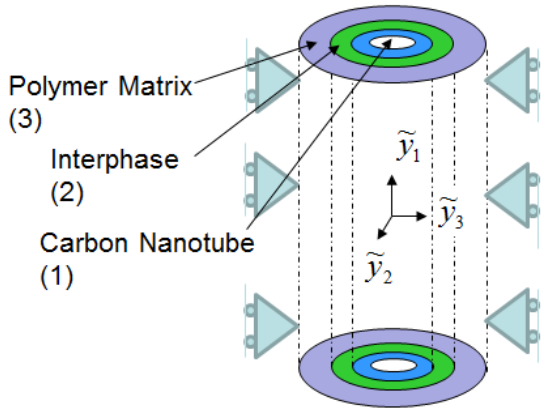

Figure 4: Composite Cylinder Assemblage

Geometric data from Ruoff et al (Ref. [41]) is utilized for the dimensions of the CNT. The CNT therefore has an outer radius of 0.85 nm and an annular thickness of 0.34 nm. The annular thickness value is observed as the interlayer spacing of graphite and multi-walled carbon nanotubes. The interphase thickness is taken to be equal to the annular thickness of the nanotube. The matrix thickness is variable depending on the volume fraction. The composite cylinders approach first assumes a displacement field in each layer of the assemblage as shown in Eqns. 2.7a - 2.7c, where $B_1^{(i)}$ and $B_2^{(i)}$ are constants and (i) indicates the phase (1=CNT, 2=Interphase, and 3=matrix). This displacement field satisfies the equilibrium equations in cylindrical coordinates, and the constants are calculated with boundary conditions and matching conditions. The displacement field constants contain information about the boundary conditions, material properties, and geometric properties. The tilde (~) represents quantities in the local nanoscale RVE coordinate system.

$$\tilde{u}_\theta^{(i)} = 0 \tag{2.7a}$$

$$\tilde{u}_r^{(i)} = B_1^{(i)} r + B_2^{(i)} \frac{1}{r} \tag{2.7b}$$

$$\tilde{u}_z^{(i)} = 0 \tag{2.7c}$$

The strain-displacement relations are then used to calculate the non-trivial elastic strain for each layer in the assemblage as seen in Eqns. 2.8a - 2.8c. The coefficient of thermal expansion is assumed to have at most transversely isotropic material symmetry in each phase. Note that $\tilde{\alpha}_{22} = \tilde{\alpha}_{rr} = \tilde{\alpha}_{\theta\theta}$ in this context for the assumed transversely isotropic material response.

$$^{\mathrm{El}}\tilde{\epsilon}_{rr}^{(i)} = \frac{\partial \tilde{u}_r^{(i)}}{\partial r} - \tilde{\alpha}_{22}\Delta T \tag{2.8a}$$

$$^{\mathrm{El}}\tilde{\epsilon}_{\theta\theta}^{(i)} = \frac{\tilde{u}_r^{(i)}}{r} - \tilde{\alpha}_{22}\Delta T \tag{2.8b}$$

$$^{\mathrm{El}}\tilde{\epsilon}_{zz}^{(i)} = -\tilde{\alpha}_{11}\Delta T \tag{2.8c}$$

Isotropic linear elastic constitutive relations are then used to determine the non-trivial stresses in each layer as seen in Eqns. 2.9a - 2.9c,

$$\tilde{\sigma}_{rr}^{(i)} = 2\tilde{\mu}^{(i)\mathrm{El}}\tilde{\epsilon}_{rr}^{(i)} + \tilde{\lambda}^{(i)\mathrm{El}}\tilde{\epsilon}_{kk}^{(i)} \tag{2.9a}$$

$$\tilde{\sigma}_{\theta\theta}^{(i)} = 2\tilde{\mu}^{(i)\mathrm{El}}\tilde{\epsilon}_{\theta\theta}^{(i)} + \tilde{\lambda}^{(i)\mathrm{El}}\tilde{\epsilon}_{kk}^{(i)} \tag{2.9b}$$

$$\tilde{\sigma}_{zz}^{(i)} = 2\tilde{\mu}^{(i)\mathrm{El}}\tilde{\epsilon}_{zz}^{(i)} + \tilde{\lambda}^{(i)\mathrm{El}}\tilde{\epsilon}_{kk}^{(i)} \tag{2.9c}$$

where μ and λ are the Lamé constants and $^{\mathrm{El}}\tilde{\epsilon}_{kk}^{(i)}$ is given by Eqn. 2.10.

$$^{\mathrm{El}}\tilde{\epsilon}_{kk}^{(i)} = ^{\mathrm{El}}\tilde{\epsilon}_{rr}^{(i)} + ^{\mathrm{El}}\tilde{\epsilon}_{\theta\theta}^{(i)} + ^{\mathrm{El}}\tilde{\epsilon}_{zz}^{(i)} \tag{2.10}$$

The displacement field constants are then determined by use of boundary and interface matching conditions. The boundary conditions for the thermal expansion problem are stated in Eqn. 2.11, where r_0 is the inner radius of the CNT and r_3 is the outer radius of the matrix. Eqn. 2.11a constrains the outer surface from expanding due to the temperature change, and Eqn. 2.11b states that the internal CNT faces are to remain traction free.

$$\tilde{u}_r^{(3)}(z, r = r_3, \theta) = 0 \tag{2.11a}$$

$$\tilde{\sigma}_{rr}^{(1)}(z, r = r_0, \theta) = 0 \tag{2.11b}$$

The interface matching conditions are given in Eqn. 2.12. Eqn. 2.12a requires the continuity of displacements at the layer boundaries, and Eqn. 2.12b requires the continuity of tractions at the layer boundaries (perfect bonding).

$$\tilde{u}_r^{(j)}(z, r = r_j, \theta) = \tilde{u}_r^{(j+1)}(z, r = r_j, \theta) \tag{2.12a}$$

$$\tilde{\sigma}_{rr}^{(j)}(z, r = r_j, \theta) = \tilde{\sigma}_{rr}^{(j+1)}(z, r = r_j, \theta) \tag{2.12b}$$

The effective properties of the nanoscale RVE are expected to have transversely isotropic material symmetry, so the effective axial ($\tilde{\alpha}_{11}^{\text{eff}}$) and transverse ($\tilde{\alpha}_{22}^{\text{eff}}$) coefficient of thermal expansion components are obtained by solving the equations

$$\begin{aligned}
\langle\tilde{\sigma}_{11}\rangle &= \left(2\tilde{\kappa}_{23}^{\text{eff}}\tilde{\nu}_{12}^{\text{eff}}\right)\left(\langle^{\text{Tot}}\tilde{\epsilon}_{22}\rangle - \tilde{\alpha}_{22}^{\text{eff}}\Delta T\right) \\
&\quad + \left(2\tilde{\kappa}_{23}^{\text{eff}}\tilde{\nu}_{12}^{\text{eff}}\right)\left(\langle^{\text{Tot}}\tilde{\epsilon}_{33}\rangle - \tilde{\alpha}_{22}^{\text{eff}}\Delta T\right) \\
&\quad + \left(\tilde{E}_{11}^{\text{eff}} + 4\left(\tilde{\nu}_{12}^{\text{eff}}\right)^2\tilde{\kappa}_{23}^{\text{eff}}\right)\left(\langle^{\text{Tot}}\tilde{\epsilon}_{11}\rangle - \tilde{\alpha}_{11}^{\text{eff}}\Delta T\right) \\
\langle\tilde{\sigma}_{22}\rangle &= \left(\tilde{\kappa}_{23}^{\text{eff}} + \tilde{\mu}_{23}^{\text{eff}}\right)\left(\langle^{\text{Tot}}\tilde{\epsilon}_{22}\rangle - \tilde{\alpha}_{22}^{\text{eff}}\Delta T\right) \\
&\quad + \left(\tilde{\kappa}_{23}^{\text{eff}} - \tilde{\mu}_{23}^{\text{eff}}\right)\left(\langle^{\text{Tot}}\tilde{\epsilon}_{33}\rangle - \tilde{\alpha}_{22}^{\text{eff}}\Delta T\right) \\
&\quad + \left(2\tilde{\kappa}_{23}^{\text{eff}}\tilde{\nu}_{12}^{\text{eff}}\right)\left(\langle^{\text{Tot}}\tilde{\epsilon}_{11}\rangle - \tilde{\alpha}_{11}^{\text{eff}}\Delta T\right)
\end{aligned} \tag{2.13}$$

where the $\langle\bullet\rangle$ denotes volume averages of the stress and total strain over the composite cylinder assemblage expressed in cartesian coordinates, and where $\tilde{\kappa}_{23}^{\text{eff}}$, $\tilde{\mu}_{23}^{\text{eff}}$, $\tilde{E}_{11}^{\text{eff}}$ and $\tilde{\nu}_{12}^{\text{eff}}$ are the in-plane bulk modulus, in-plane shear modulus, axial Young's modulus, and axial Poisson's ratio, respectively. These effective mechanical properties are determined from isothermal composite cylinders solutions as summarized in Ref. [5]. The

solution of Eqn. 2.13 for $\tilde{\alpha}_{11}^{\text{eff}}$ and $\tilde{\alpha}_{22}^{\text{eff}}$ yields:

$$\begin{aligned}
\tilde{\alpha}_{11}^{\text{eff}} &= \frac{1}{\tilde{E}_{11}^{\text{eff}}\Delta T}(\tilde{E}_{11}^{\text{eff}}\langle^{\text{Tot}}\tilde{\epsilon}_{11}\rangle - \langle\tilde{\sigma}_{11}\rangle + 2\tilde{\nu}_{12}^{\text{eff}}\langle\tilde{\sigma}_{22}\rangle \\
&\quad + 2\tilde{\nu}_{12}^{\text{eff}}\tilde{\mu}_{23}^{\text{eff}}\left(\langle^{\text{Tot}}\tilde{\epsilon}_{33}\rangle - \langle^{\text{Tot}}\tilde{\epsilon}_{22}\rangle\right)) \\
\tilde{\alpha}_{22}^{\text{eff}} &= \frac{1}{2\tilde{E}_{11}^{\text{eff}}\tilde{\kappa}_{23}^{\text{eff}}\Delta T}[2\tilde{\kappa}_{23}^{\text{eff}}\langle\tilde{\sigma}_{11}\rangle \\
&\quad - \left(\tilde{E}_{11}^{\text{eff}} + 4\left(\tilde{\nu}_{12}^{\text{eff}}\right)^2\tilde{\kappa}_{23}^{\text{eff}}\right)\langle\tilde{\sigma}_{22}\rangle \\
&\quad + \left(\tilde{E}_{11}^{\text{eff}}\left(\tilde{\kappa}_{23}^{\text{eff}} + \tilde{\mu}_{23}^{\text{eff}}\right) + 4\left(\tilde{\nu}_{12}^{\text{eff}}\right)^2\tilde{\kappa}_{23}^{\text{eff}}\tilde{\mu}_{23}^{\text{eff}}\right)\langle^{\text{Tot}}\tilde{\epsilon}_{22}\rangle \\
&\quad + \left(\tilde{E}_{11}^{\text{eff}}\left(\tilde{\kappa}_{23}^{\text{eff}} - \tilde{\mu}_{23}^{\text{eff}}\right) - 4\left(\tilde{\nu}_{12}^{\text{eff}}\right)^2\tilde{\kappa}_{23}^{\text{eff}}\tilde{\mu}_{23}^{\text{eff}}\right)\langle^{\text{Tot}}\tilde{\epsilon}_{33}\rangle]
\end{aligned} \tag{2.14}$$

2.2 Mori-Tanaka Method

2.2.1 Eshelby Solution for Aligned Fibers

The Mori-Tanaka method is an analytical technique used to calculate effective properties by determining concentration tensors. The full derivation can be found in Ref. [42]. The Mori-Tanaka method allows for modeling of random orientation of phases in a composite and for modeling of multiple types of fibers, unlike the CCM model discussed in Section 2.1. However, this method can only account for ellipsoidal inclusions, and it only accounts for fiber interactions implicitly (instead of explicitly as will be shown in the finite element method model). A linear elastic matrix material that contains homogeneous ellipsoidal ihomogeneities can utilize the Eshelby tensor in order to solve for strain concentration tensors as seen in Eqn. 2.15, where $\tilde{T}$, I, S^{cyl}, L^M, and $\tilde{L}^{CNT}$ are the strain concentration tensor, the identity tensor, the Eshelby solution for a cylinder, the matrix stiffness, and the CNT stiffness respectively.

$$\tilde{T}_{ijkl}^J = \left\{I_{lkji} + S_{ijkl}^J(L_{qpnm}^M)^{-1}(\tilde{L}_{mnji}^J - L_{mnji}^M)\right\}^{-1} \tag{2.15}$$

The tilde (∼) represents quantities in the local nanoscale RVE coordinate system. Stiffness properties are related to the stress tensor and the infinitesimal strain tensor as seen in Eqn. 2.16. Note that this material symmmetry is for an orthotropic material.

$$\begin{Bmatrix} \sigma_{11} \\ \sigma_{22} \\ \sigma_{33} \\ \sigma_{23} \\ \sigma_{13} \\ \sigma_{12} \end{Bmatrix} = \begin{bmatrix} L_{1111} & L_{1122} & L_{1133} & 0 & 0 & 0 \\ L_{1122} & L_{2222} & L_{2233} & 0 & 0 & 0 \\ L_{1133} & L_{2233} & L_{3333} & 0 & 0 & 0 \\ 0 & 0 & 0 & L_{2323} & 0 & 0 \\ 0 & 0 & 0 & 0 & L_{1313} & 0 \\ 0 & 0 & 0 & 0 & 0 & L_{1212} \end{bmatrix} \begin{Bmatrix} \epsilon_{11} \\ \epsilon_{22} \\ \epsilon_{33} \\ 2\epsilon_{23} \\ 2\epsilon_{13} \\ 2\epsilon_{12} \end{Bmatrix} \tag{2.16}$$

The inverse of Eqn. 2.16 allows the stress tensor and the infinitesimal strain tensor to be related through the compliance tensor as shown in Eqn. 2.17.

$$\begin{Bmatrix} \epsilon_{11} \\ \epsilon_{22} \\ \epsilon_{33} \\ 2\epsilon_{23} \\ 2\epsilon_{13} \\ 2\epsilon_{12} \end{Bmatrix} = \begin{bmatrix} \frac{1}{E_{11}} & -\frac{\nu_{21}}{E_{22}} & -\frac{\nu_{31}}{E_{33}} & 0 & 0 & 0 \\ -\frac{\nu_{12}}{E_{11}} & \frac{1}{E_{22}} & -\frac{\nu_{32}}{E_{33}} & 0 & 0 & 0 \\ -\frac{\nu_{13}}{E_{11}} & -\frac{\nu_{23}}{E_{22}} & \frac{1}{E_{33}} & 0 & 0 & 0 \\ 0 & 0 & 0 & \frac{1}{\mu_{23}} & 0 & 0 \\ 0 & 0 & 0 & 0 & \frac{1}{\mu_{13}} & 0 \\ 0 & 0 & 0 & 0 & 0 & \frac{1}{\mu_{12}} \end{bmatrix} \begin{Bmatrix} \sigma_{11} \\ \sigma_{22} \\ \sigma_{33} \\ \sigma_{23} \\ \sigma_{13} \\ \sigma_{12} \end{Bmatrix} \tag{2.17}$$

The micromechanics problem here involves representing a matrix with ellipsoidal inhomogeneities with an equivalent homogeneous material. Each inhomogeneity is placed in an infinite elastic medium and is subjected to an eigenstrain. The Eshelby solution starts by removing the inclusion from the medium to allow it to undergo this eigenstrain. A surface traction is then applied to the inclusion that accounts for the eigenstrain, and it is placed back into the elastic medium. This surface traction is then replaced by an opposite traction on the surface of the inclusion in the matrix. It is then possible to solve the boundary value problem in order to determine the stress and strain state created by the eigenstrain. The constrained strain, ϵ^*, is related to the uniform total strain in the composite by the Eshelby solution as shown in Eqn. 2.18 [43].

$$\epsilon = \mathbf{S}\epsilon^* \tag{2.18}$$

The Eshelby solution is governed by the shape and the material properties of the matrix material. The Eshelby tensor can be seen in Eqn. 2.19.

$$\mathbf{S} = \begin{pmatrix} S_{1111} & S_{1122} & S_{1133} & 0 & 0 & 0 \\ S_{2211} & S_{2222} & S_{2233} & 0 & 0 & 0 \\ S_{3311} & S_{3322} & S_{3333} & 0 & 0 & 0 \\ 0 & 0 & 0 & 2S_{1212} & 0 & 0 \\ 0 & 0 & 0 & 0 & 2S_{1313} & 0 \\ 0 & 0 & 0 & 0 & 0 & 2S_{2323} \end{pmatrix} \tag{2.19}$$

Effective nanofibers can be represented by infinitely long circular cylinders, and the Eshelby tensor components for this type of inclusion can be seen in Eqn. 2.20, where ν is Poisson's ratio.

$$\begin{aligned} S_{1111} &= S_{2222} = \frac{5-4\nu}{8(1-\nu)} \\ S_{3333} &= S_{3311} = S_{3322} = 0 \\ S_{1122} &= S_{2211} = \frac{4\nu-1}{8(1-\nu)} \\ S_{1133} &= S_{2233} = \frac{\nu}{2(1-\nu)} \\ S_{1212} &= \frac{3-4\nu}{8(1-\nu)} \\ S_{1313} &= S_{2323} = \frac{1}{4} \end{aligned} \tag{2.20}$$

The strain concentration tensor is identified in the Mori-Tanaka approach, and the concentration tensor, A, is calculated for each phase in the composite by use of Eqn. 2.21,

$${}^{MT}A^J_{ijkl} = T^J_{ijpq}\left\{\left(1-\sum_{R=1}^{N-1} c_R\right) I_{klpq} + \sum_{R=1}^{N-1} c_R T^R_{klpq}\right\}^{-1} \tag{2.21}$$

where T is the dilute strain concentration tensor in the Jth phase, N is the total number of phases (including the matrix), and c_R is the volume fraction of the Rth phase. Effective stiffness for the composite can then be calculated by way of Eqn. 2.22.

$$\mathbf{L}^{\text{eff}} = \mathbf{L}^M + \sum_{J=1}^{K} c_J \left(\mathbf{L}^J - \mathbf{L}^M\right)^{MT} \mathbf{A}^J \tag{2.22}$$

The effective CTE can be solved for in a similar manner as seen in Eqn. 2.23 [44].

$$\boldsymbol{\alpha}^{\text{eff}} = \boldsymbol{\alpha}^M + \sum_{J=1}^{K} c_J \left\{ \left(\mathbf{L}^J - \mathbf{L}^M\right) \left[\mathbf{S}^J - \sum_{J=1}^{K} c_J \left(\mathbf{S}^J - \mathbf{I}\right) \right] + \mathbf{L}^M \right\}^{-1} \mathbf{L}^J \left(\boldsymbol{\alpha}^J - \boldsymbol{\alpha}^M\right) \tag{2.23}$$

2.2.2 Accounting for Randomly Oriented Fibers

Random orientation of the fibers was also modeled treating each origination as a separate J phase. The phases are then summed over all orientations using a continuous normalized distribution of orientations. The strain concentration tensor, A, for randomly oriented fibers is calculated using the Mori-Tanaka Method shown in Eqn. 2.24.

$$A_{ijkl}^{MT}(\psi,\phi) = Q_{im}Q_{jn}\tilde{T}_{mnpq}^{CNT}Q_{rp}Q_{sq} \left\{ (1-c_f)I_{klrs} + \frac{c_f}{4\pi}\int_0^{2\pi}\int_0^{\pi} Q_{kt}Q_{lu}\tilde{T}_{tuvw}^{CNT}Q_{rv}Q_{sw}\sin(\phi)d\phi d\psi \right\}^{-1} \tag{2.24}$$

The effective stiffness for randomly oriented fibers is determined by way of Eqn. 2.25.

$$\mathbf{L}^{\text{eff}} = \mathbf{L}^M + \frac{c_f}{4\pi}\int_0^{2\pi}\int_0^{\pi} \left(\mathbf{L}^{CNT} - \mathbf{L}^M\right)\mathbf{A}^{MT}\sin(\phi)d\phi\psi \tag{2.25}$$

Note that the quantities in Eqn. 2.25 are given in terms of the microscale coordinate system, y_i. 3-1-3 Euler angle rotation matrices, $Q_{ij}\left(\psi, \pi/2, \phi\right)$, are used to relate these microscale quantities to the local nanoscale RVE coordinate system, $\tilde{y}_i$ as shown in Eqn. 2.26.

$$L_{ijkl}^{CNT}(\psi,\phi) = Q_{im}Q_{jn}\tilde{L}_{mnpq}^{CNT}Q_{kp}Q_{lq} \tag{2.26}$$

The concentration tensor, B, needed for calculating effective CTE for randomly oriented fibers is calculated using the Mori-Tanaka method as shown in Eqn. 2.27,

$$B_{ijkl}^{CNT-MT0}(\psi,\phi) = Q_{im}Q_{jn}\tilde{P}_{mnpq}^{CNT}Q_{rp}Q_{sq}\left\{(1-c_f)I_{klrs} + \frac{c_f}{4\pi}\int_0^{2\pi}\int_0^{\pi} Q_{kt}Q_{lu}\tilde{P}_{tuvw}^{CNT}Q_{rv}Q_{sw}\sin(\phi)d\phi d\psi\right\}^{-1} \tag{2.27}$$

where $\tilde{P}$ is calculated using Eqn. 2.28.

$$\tilde{P}_{ijkl}^{CNT} = \tilde{L}_{ijmn}^{CNT}\tilde{T}_{mnpq}^{CNT}\tilde{M}_{pqkl}^{CNT} \tag{2.28}$$

Effective CTE for randomly oriented fibers can then be computed by way of Eqn. 2.29.

$$\boldsymbol{\alpha}^{\text{eff}} = \frac{1}{4\pi}\int_0^{2\pi}\int_0^{\pi}\left\{(1-c_f)\,\boldsymbol{\alpha}^{M}\mathbf{B}^{M-MT0} + c_f\boldsymbol{\alpha}^{CNT}\mathbf{B}^{CNT-MT0}\right\}\sin(\phi)\,d\phi d\psi \tag{2.29}$$

It is noted that the quantities in Eqn. 2.29 are given in terms of the microscale coordinate system, y_i. 3-1-3 Euler angle rotation matrices, $Q_{ij}(\psi,\pi/2,\phi)$, are used to relate these microscale quantities to the local nanoscale RVE coordinate system, $\tilde{y}_i$ as shown in Eqn. 2.30.

$$\alpha_{ij}^{CNT}(\psi,\phi) = Q_{im}\tilde{\alpha}_{mn}^{CNT}Q_{jn} \tag{2.30}$$

2.3 Computational Micromechanics Model for Effective Coefficient of Thermal Expansion

The finite element formulation described herein allows for modeling of more complex geometries (such as clustering and clustering with interphase). The finite element formulation also accounts for interactions

between the CNTs explicitly. The CCM model can only model circular shapes and the Mori-Tanaka method with the Eshelby solution can only model ellipsoidal inclusions. Verification of the finite element model with the CCM and Mori-Tanaka models gives confidence that the finite element model can be utilized for the more complex geometries. The computational micromechanics nanoscale RVE consists of a periodic hexagonal array of CNTs as shown in Figure 5. Transversely isotropic effective properties are expected, and the hexagonal array of CNTs is shown to produce transversely isotropic effective material properties [45, 46]. Solid and hollow configurations were both created, and the material properties for both can be seen in Table 1. RVEs are created at several volume fractions using Eqns. 2.31 - 2.33, where r is the radius of

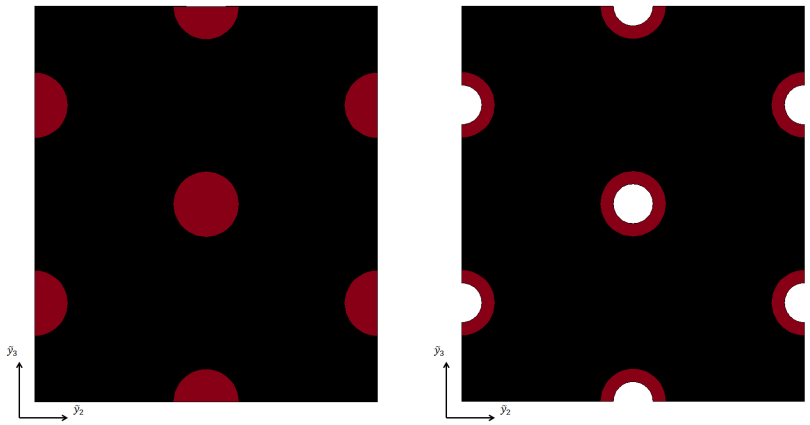

(a) Effective solid nanofiber (b) Hollow nanotube

Figure 5: Solid and hollow representations of hexagonal packing array at $V_f = 0.1$.

the fiber and l represents the length between the center of one fiber and the center of one of the other six surrounding fibers. The radius, r, of the fiber is the same outer radius of the CNT shown in Section 2.1 for the CCM method. Note that r of the CNT does not change with volume fraction as shown in Figure 6.

$$V_f = \frac{\pi r^2}{l^2 \cos(30)} \tag{2.31}$$

$$L = l + 2\sin(\theta) = 2l \tag{2.32}$$

$$W = 2l\cos(\theta) \tag{2.33}$$

The three-dimensional computational domain consists of on the order of 50 thousand tetrahedral elements,

Table 1: Table of material properties for the polymer matrix, CNT, and effective nanofiber [4, 5, 6]

Matrix		CNT	
E	2.97 GPa	$\tilde{E}$	1100 GPa
ν	0.36	$\tilde{\nu}$	0.14
α_{11}	6.08E-05 $/^\circ K$	$\tilde{\alpha}_{11}$	1.50E-06 $/^\circ K$
α_{22}	6.08E-05 $/^\circ K$	$\tilde{\alpha}_{22}$	7.50E-06 $/^\circ K$
Effective Nanofiber			
$\tilde{E}_{11}$	704 GPa	$\tilde{\kappa}_{23}$	286 GPa
$\tilde{\nu}_{12}$	0.14	$\tilde{\mu}_{12}$	227 GPa
$\tilde{\alpha}_{11}$	1.50E-06 $/^\circ K$	$\tilde{\mu}_{23}$	125 GPa
$\tilde{\alpha}_{22}$	1.13E-05 $/^\circ K$	-	-

with on the order of 10 elements through the thickness (i.e. in the CNT axis direction) as seen in Figure 7. The boundary and interface matching conditions consist of stress free internal CNT surfaces, constrained outer boundary displacements, and continuity of displacements and tractions along interface boundaries between phases. The Structural Mechanics Module of Comsol 3.4 is used to compute the displacement field in the RVE resulting from the application of a nominal ΔT. The volume averaged stress and total strain are then obtained from the post-processed data and are used to solve for the axial and transverse coefficients of thermal expansion using Eqn. 2.14 in cartesian coordinates form, with effective elastic properties for the nanocomposite provided by the composite cylinder method[2].

[2]In Ref. [34] it was observed that the composite cylinders and finite element based computational micromechanics approaches gave similar results for the elastic properties of nanocomposites.

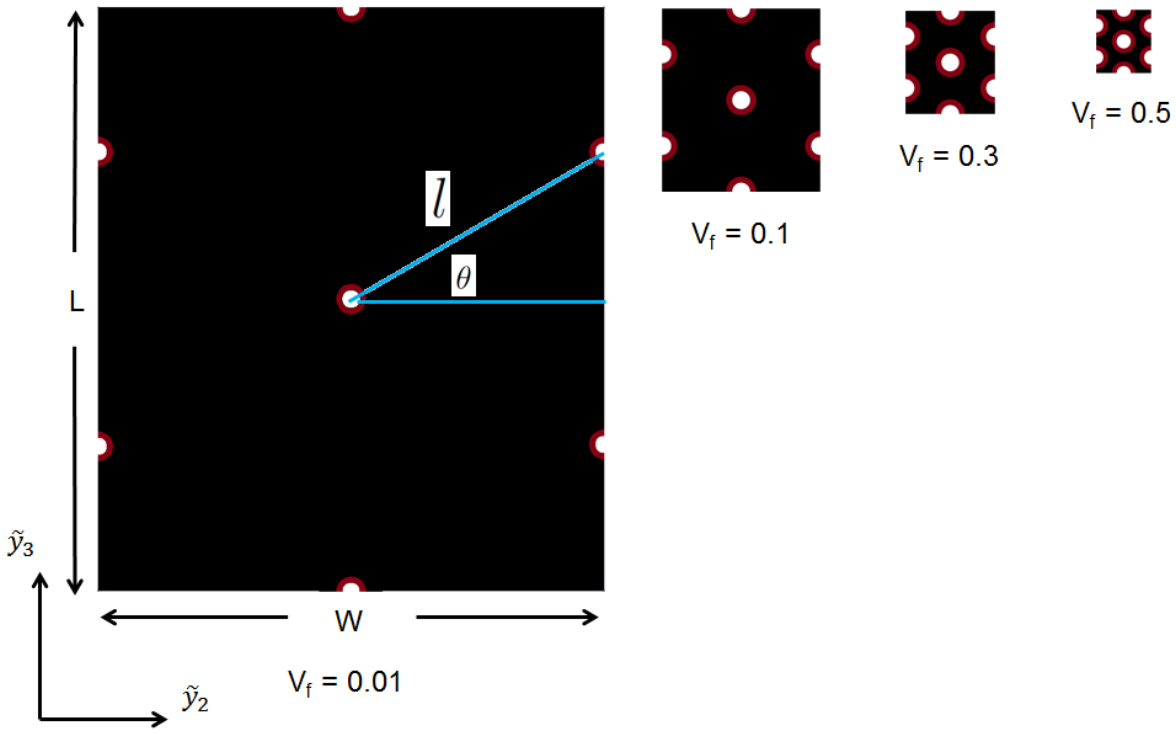

Figure 6: RVEs of several volume fractions.

2.4 Computational Micromechanics Model for Interphase Layer

An interphase layer was added between the matrix and each nanotube in the nanoscale RVE as shown in Figure 8. The interphase layer thickness is kept constant with differing volume fractions. Interphase layers are added in order to represent the perturbation of the polymer due to the presence of the nanotubes. The influence of an interphase region on the effective CTE components was explored in a parametric study on interphase properties using a 0.34nm thick interphase region[3]. This 0.34nm thickness corresponds to the annular thickness of each nanotube. The interphase elastic and thermoelastic properties are varied in three cases: i) an increase in elastic stiffness by a factor of 10 relative to the matrix stiffness (labeled 10E), ii) an increase in CTE of a factor of 10 relative to the matrix CTE (labeled 10a), and iii) an increase of both a

[3]The value for interphase thickness was selected to be consistent with previous studies [5] which has selected the value based on TEM images of nanotube pull-out from a polymer matrix.

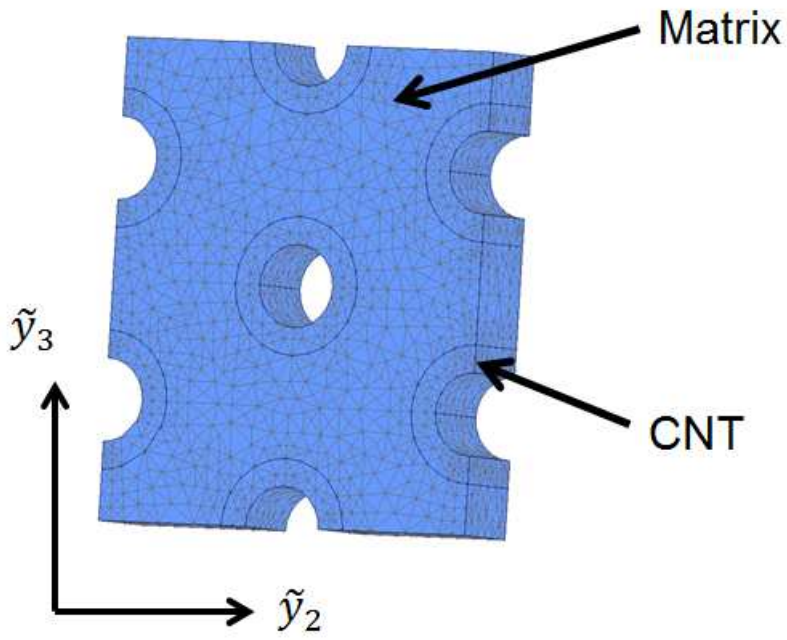

Figure 7: Meshed well-dispersed RVE at $V_f = 0.1$.

factor of 10 in stiffness and in CTE relative to the matrix (labeled 10Ea). The exact material properties of the interphase layer are not know, so the parametric study is done to evaluate the important of an interphase region on the effective CTE. The addition of an interphase region will lead to what is termed an interphase percolation as the volume fraction is increased to the interphase percolation volume fraction. As the volume fraction is increased, the interphase regions of neighboring nanotubes come into contact and begin to overlap one another as shown in Figure 9. It is noted that the composite cylinder method cannot be used at volume fractions with this overlap as the RVE now contains non-circular regions. The Mori-Tanaka method with the Eshelby solution cannot be used either as the inclusions are not ellipsoidal. The 3-phase (nanotube, interphase, matrix) RVE transitions to a 2-phase (nanotube, interphase) RVE as the volume fraction is further increased as seen in Figure 9 . The composite cylinders method can again be used for this 2-phase material. The Structural Mechanics Module of Comsol 3.4 is again used to compute the displacement field in the RVE due to the nominal ΔT.

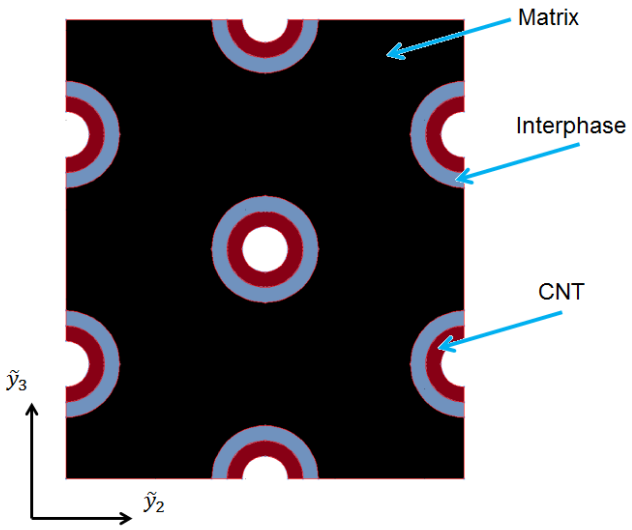

Figure 8: Interphase Region

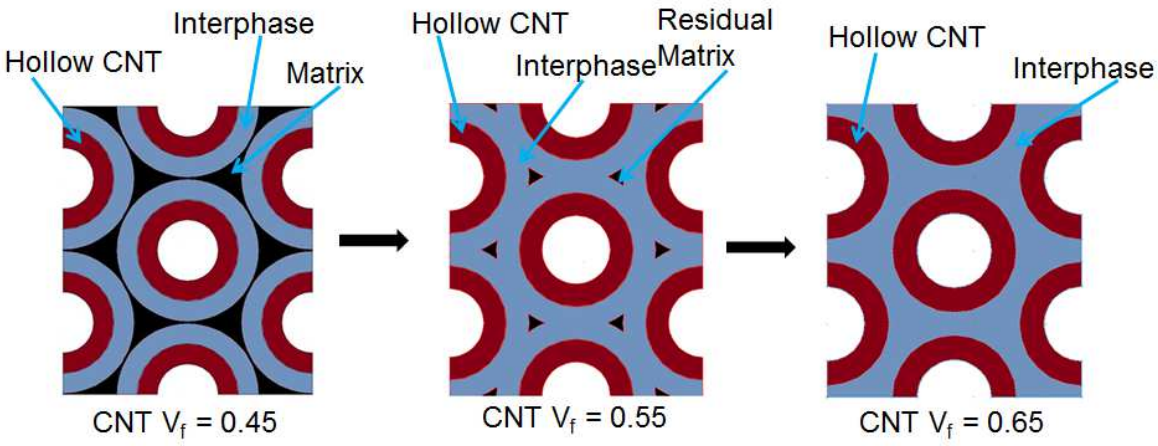

Figure 9: Transition from 3-phase to 2-phase material through interphase percolation volume fraction.

2.5 Computational Micromechanics Model for Clustered RVEs

The well-dispersed configuration used for the previous RVEs is an idealization of the arrangement of nanotubes. In a practical setting, it is difficult to evenly disperse CNTs throughout a polymer matrix. CNTs will tend to cluster together due to van der Walls forces, and it is therefore important to model this phenomenon

in order to accurately predict effective CTE values for the composite [47, 48]. Different degrees of clustered RVEs are created in order to analyze the effect of nanotube bundling. First, a larger RVE is created using symmetry to create an RVE consisting of 36 hollow nanotubes as seen in Figure 10. A volume fraction of

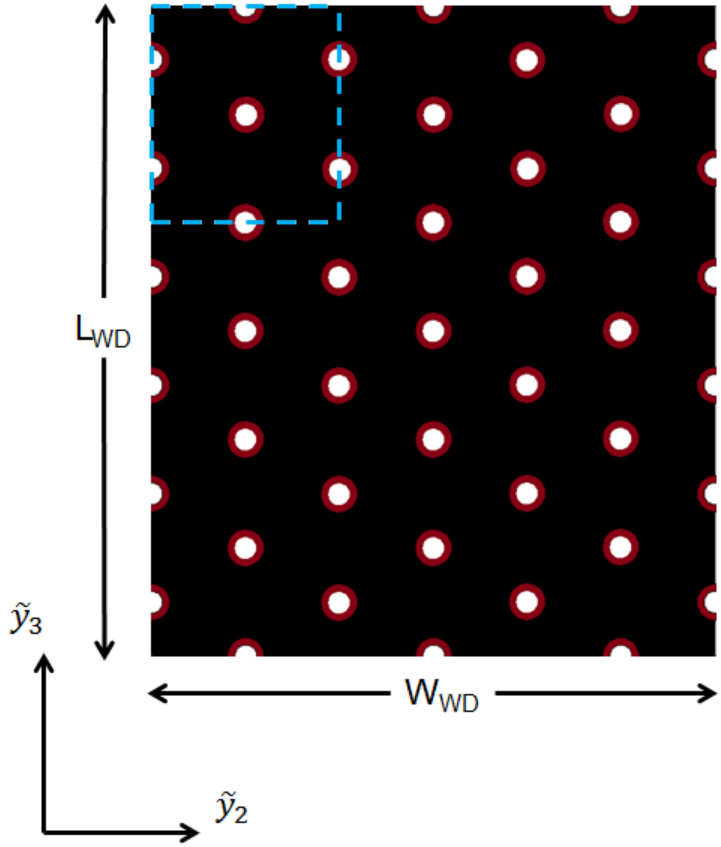

Figure 10: Step 0 clustered configuration at $V_f = 0.1$.

0.1 is then chosen as the baseline position of nanotubes for the new cluster configurations. The dimensions of the RVE box are kept constant, and the nanotubes are bundled in four successive steps by changing the position of each nanotube as seen in Figure 11. The four cluster steps are labeled as Step 1 (least amount of clustering, Figure 11a) through Step 4 (most amount of clustering without contact between nanotubes, Figure 11d). This clustering process presents the addition of 9 more hollow nanotubes, bringing the total to 45 effective nanotubes. The dimensions of the box are recalculated using Equation 2.34 and Equation 2.38.

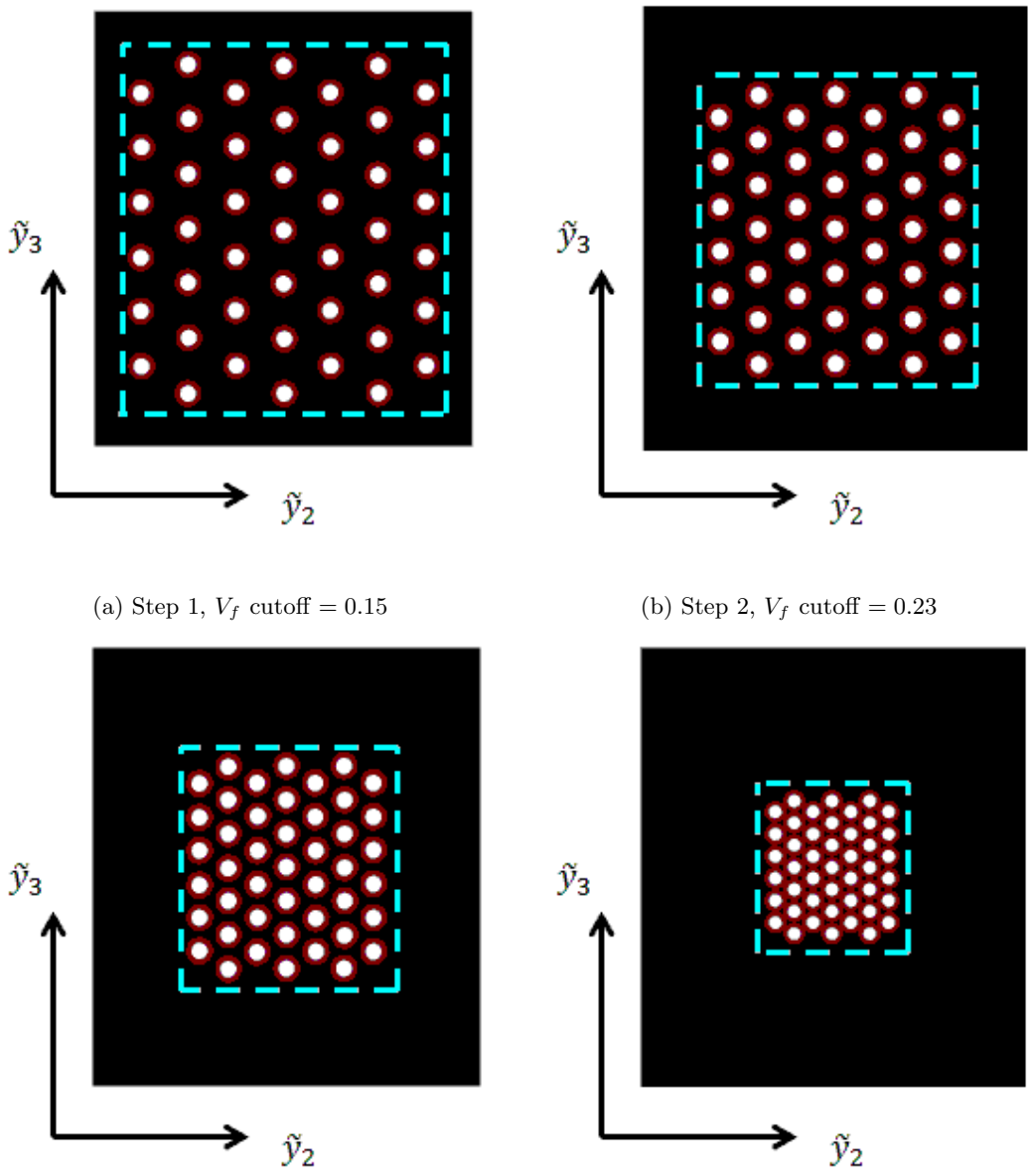

(a) Step 1, V_f cutoff = 0.15

(b) Step 2, V_f cutoff = 0.23

(c) Step 3, V_f cutoff = 0.38

(d) Step 4, V_f cutoff = 0.78

Figure 11: Clustering Steps 1-4 at $V_f = 0.1$.

$$V_f = \frac{45\pi r^2}{LW} \tag{2.34}$$

$$L = l + 2\sin(\theta) = 2l \tag{2.35}$$

$$W = 2l\cos(\theta) \tag{2.36}$$

$$\theta = 30^{\circ} \tag{2.37}$$

$$AR = \frac{L_{WD}}{W_{WD}} \tag{2.38}$$

AR is the aspect ratio of the non-clustered configuration seen in Figure 10. The volume fraction for each clustered step is varied by changing the dimensions of the box while the nanotube positions are kept fixed. Cutoff maximum volume fractions are shown with the dashed lines, and represent the maximum volume fraction for that cluster step.

Six sets of periodic boundary conditions are applied to each RVE in the same fashion as seen in Ref. [13] in order to solve for the mechanical properties and necessary volume averaged field quantities at each volume fraction for calculating effective CTE values of the composite. Periodic boundary conditions allow for the RVE to be modeled as an infinite medium with some far field displacement on the boundary. For example, an extension in the x-direction is applied with peridoic boundary conditions as seen in Eqn. 2.39,

$$u_{\tilde{y}_2}\left(L^0_{\tilde{y}_2}/2, \tilde{y}_3, \tilde{y}_1\right) = u_{\tilde{y}_2}\left(-L^0_{\tilde{y}_2}/2, \tilde{y}_3, \tilde{y}_1\right) + \epsilon^0 L^0_{\tilde{y}_2} \tag{2.39}$$

where u is the x-component of displacement, L^0_x is the original undeformed length along the x-direction of the RVE, ϵ^0 is the applied strain, and $u_{re} = \epsilon^0 L^0_x$ is the relative displacement. A nominal ΔT is then applied to each RVE. The internal CNT boundaries are left traction free, and the other boundaries are constrained. The volume averaged field quantities necessary to solve Eqn. 2.14 are then calculated.

2.6 Computational Micromechanics Model for Clustered with Interphase RVEs

An interphase layer was added to the four bundled configurations presented in Section 2.5 as shown in Figure 12. The same parametric study discussed in Section 2.4 is done to analyze the combined effects of clustering and interphase layers. It is noted that only cluster Step 4 presents an interphase percolation event as the interphase layers overlap as seen in Figure 12d.

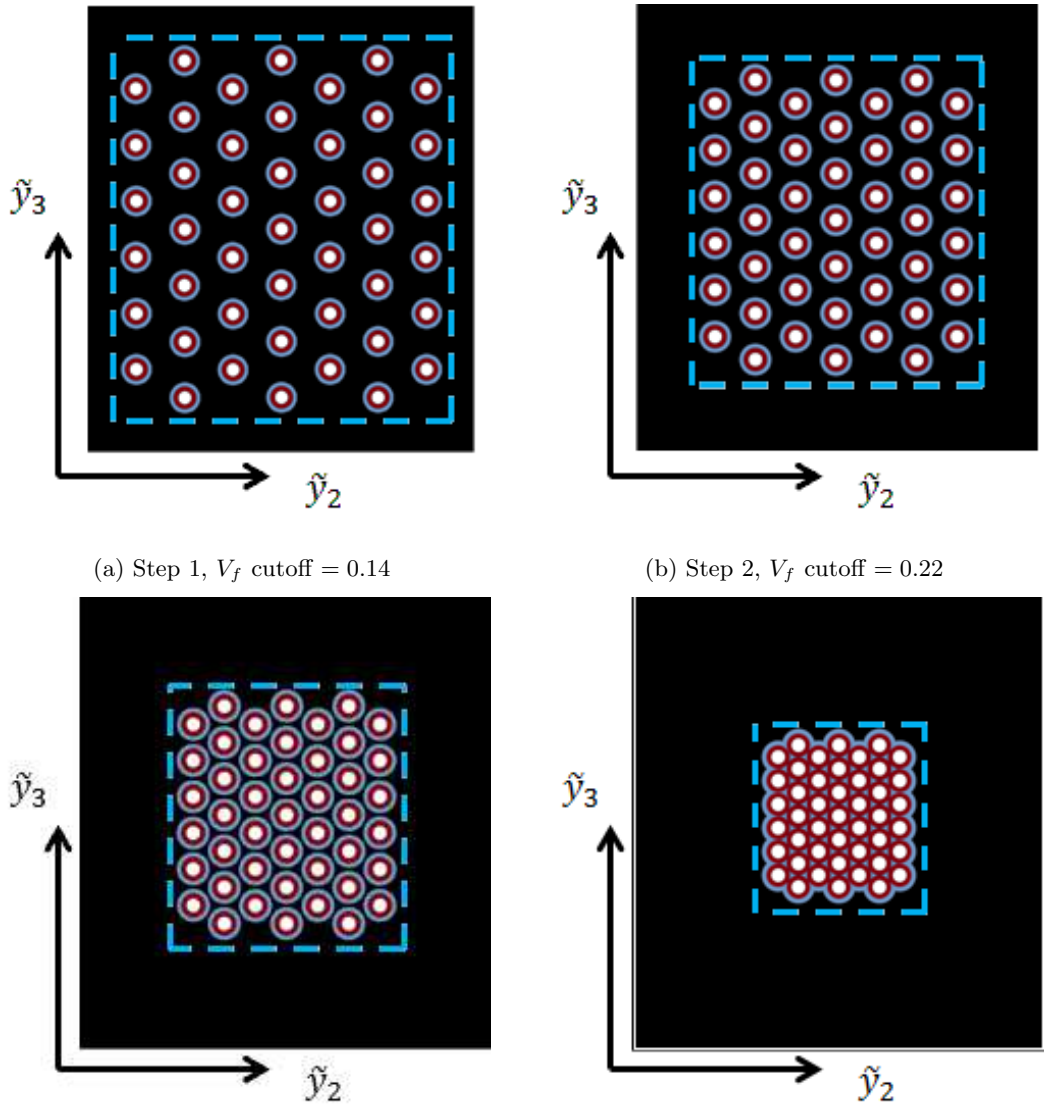

(a) Step 1, V_f cutoff = 0.14

(b) Step 2, V_f cutoff = 0.22

(c) Step 3, V_f cutoff = 0.36

(d) Step 4, V_f cutoff = 0.74

Figure 12: Clustering with Interphase Steps 1-4 at $V_f = 0.1$.

2.7 Computational-Mori-Tanaka Hybrid Model

A hybrid model of a computational and an analytical technique is utilized in order to predict effective stiffness and CTE for RVEs with clustering and clustering with interphase regions. The hybrid model allows for random orientation calculations of clustering and clustering with interphase geometries. The computational RVEs are described in more detail in Sections 2.4, 2.5, and 2.6. Strain concentration tensors were calculated for each phase in the RVE by way of Eqn. 2.40.

$$\epsilon_{ij}^{J} = T_{ijkl}^{J} \bar{\epsilon}_{kl} \tag{2.40}$$

Six sets of periodic boundary conditions, defined in Section 2.5, were applied to a computational RVE with a volume fraction of $V_f = 0.001$ for both a clustered and a clustered with interphase case. This allowed for the solution of the dilute strain concentration tensor to be used in the Mori-Tanaka method. Stiffness can then be calculated directly by way of Eqn. 2.21 and Eqn. 2.22. In order to solve for effective CTE using this method, it is necessary to inversely solve for an Eshelby tensor for every phase in the composite by use of Eqn. 2.41. This inverse solution is a non-conventional method as Eshelby tensors are based on inclusion shape and matrix material properties.

$$S_{ijkl}^{\text{eff}} = \left(\frac{\left(\tilde{T}_{ijkl}^{J} \right)^{-1} - I_{lkji}}{\tilde{L}_{mnji}^{J} - L_{mnji}^{M}} \right) L_{qpnm}^{M} \tag{2.41}$$

Effective CTE can then be calculated using Eqn. 2.23 for aligned fibers or Eqn. 2.29 for randomly oriented fibers.

3 Results and Discussion

3.1 Well-Dispersed, Aligned Nanotubes with No Interphase Layer

3.1.1 Effective Stiffness

Effective elastic properties are obtained using the Mori-Tanaka method with the Eshelby solution for infinitely long cylinders. The material properties for the epoxy matrix and the effective nanofiber, as shown in Table 1, are used in this simulation because the Mori-Tanaka method can only model ellipsoidal inclusions. The results for axial Young's modulus (E_{11}), transverse Young's modulus, (E_{22}), and two shear moduli (G_{12} and G_{23}) are shown in Figure 13, and are compared with results from Ref. [34].

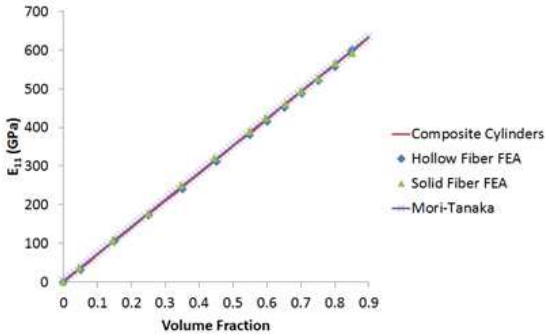

(a) Axial Young's Modulus, E_{11}

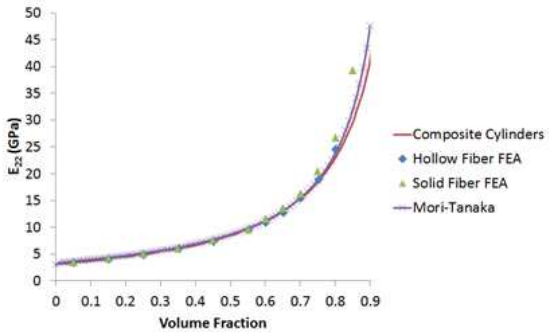

(b) Transverse Young's Modulus, E_{22}

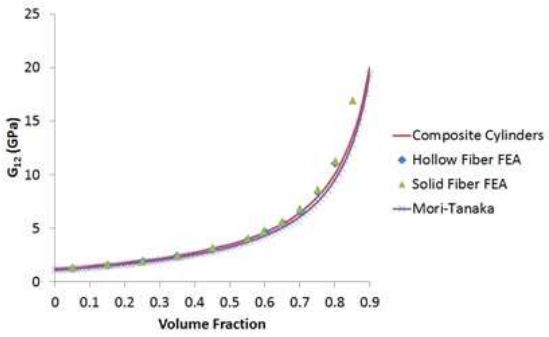

(c) Shear Modulus, G_{12}

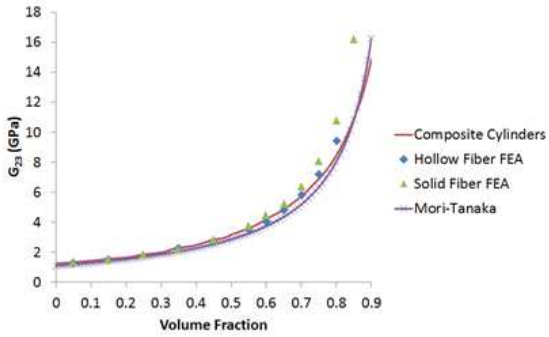

(d) Shear Modulus, G_{23}

Figure 13: Mechanical properties solved for using Mori-Tanaka method with the Eshelby solution.

The effective axial Young's modulus, E_{11}, shown in Figure 13a linearly increases with volume fraction. This trend is consistent with the general rule of mixtures for a composite material. The effective transverse Young's modulus, E_{22}, shown in Figure 13b increases with volume fraction up to $V_f = 0.6$, and then sharply increases above this volume fraction. The same E_{22} trend is seen in the effective shear moduli, G_{12} and G_{23}, as well. The effective nanofibers are aligned in the 1-direction, and this causes G_{12} to be larger than G_{23}. It is seen that the results are in good agreement with Ref. [34]. Both sets of data show a linear increase of E_{11} with volume fraction, approaching the value of the effective nanofiber (704 GPa). The transverse modulus and two shear moduli show the same trends and values in both sets of data.

The mechanical properties are calculated and compared in order to validate the Mori-Tanaka model that is implemented. The good agreement with Ref. [34] gives confidence that the Mori-Tanaka model can now be used to model effective CTE.

3.1.2 Effective Coefficient of Thermal Expansion

The effective coefficients of thermal expansion for the well-dispersed case are obtained using both analytical (composite cylinders method and Mori-Tanka method) and computational micromechanics techniques. Results for effective axial ($\tilde{\alpha}_{11}^{\text{eff}}$) and transverse ($\tilde{\alpha}_{22}^{\text{eff}}$) coefficients of thermal expansion are presented in Figure 14. Two types of CNT representations are considered in the computational micromechanics approaches, one in which the CNTs are treated as a hollow tube with isotropic properties in the annulus and the second where the CNT has been replaced by an effective nanofiber having transversely isotropic material properties obtained from a composite cylinders model.

The nanoscale RVE effective coefficients of thermal expansion correspond to the effective properties of the nanocomposite for the cases containing aligned CNTs. Therefore, a large range of volume fractions, up to $V_f = 0.9$, is provided in in order to demonstrate the comparison between the four nanoscale RVE results and will be used in Section 3.4 to assess the effects of clustering.

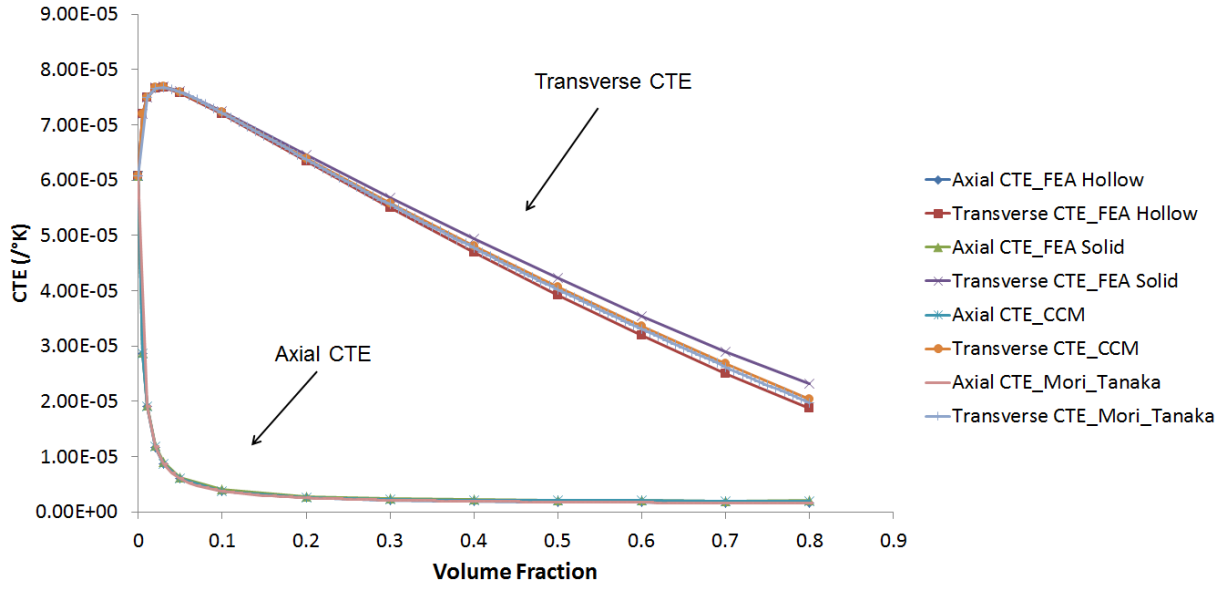

Figure 14: Nanoscale RVE effective coefficient of thermal expansion components as a function of CNT volume fraction obtained by the composite cylinder method, the Mori-Tanaka method with the Eshelby solution, and the computational micromechanics method using the hollow CNT and solid effective nanofiber representations.

The effective axial CTE shown in Figure 14 is observed to sharply decrease from the original matrix CTE value of $6.08E-05/^{\circ}K$ to a value on the order of $2E-06/^{\circ}K$. As the volume fraction reaches 0.1, the value of axial CTE has already fallen to $3.8E-06/^{\circ}K$. The CNTs are dominating the axial CTE response of the nanocomposite, and are thus causing this sharp decrease in the effective property. This type of behavior has been demonstrated for axial proeprties in other work on effective axial Young's modulus, thermal conductivity, and electrical conductivity. However, as was shown in Section 3.1.1 for effective axial Young's modulus, the predicted properties followed a the linear general rule of mixtures. Axial CTE appears to have a sharp decay towards the nanotube value of CTE rather than a linear trend. This seems to indicate that the effective CTE is being dominated by the CNT value of CTE along the tube axis.

The effective transverse CTE of the nanocomposite in Figure 14 is shown to increase to a value above the

CTE value of the matrix out to $V_f = 0.04$. It is believed that this trend is being driven by the interplay of matrix CTE and nanotube transverse elastic properties. All four methods predict this initial increase in effective transverse CTE. The transverse CTE response is then shown to decrease as the volume fraction is increased for all four models.

Relatively good agreement exists between all four models for the axial CTE response through the range of volume fractions. There is also relatively good agreement between all of the models throughout the range of volume fractions for transverse CTE. The percent difference between the FEA hollow and solid axial CTEs at a volume fraction of 0.8 is 28% and for the transverse CTEs is 24%, while the percent differences between the FEA hollow and composite cylinders method at a volume fraction of 0.8 are 27% and 9%, respectively. At a volume fraction of 0.1, the maximum of the range of epoxy-CNT nanocomposite volume fractions typically produced, the percent differences between the FEA hollow and composite cylinder model reduces to 1.5% for the axial CTE and 0.4% for the transverse CTE and continues to decrease with decreasing volume fraction. The Mori-Tanaka method is in good agreement with the other models. There is now confidence that the Mori-Tanaka model can be used to predict effective CTE for randomly oriented bundles.

Reasons for the small differences between the FEA hollow and composite cylinders solutions can be linked to small differences in the average total strain and average stress in the RVEs. The transverse ($\tilde{y}_3$-direction) displacements, normal total strains), and normal total stresses are plotted for the FEA hollow and composite cylinder cases along a radial line 30° above the x-axis (i.e., linking the centers of the center nanotube and the upper right nanotube as shown in Figure 15) for a temperature difference of $10°K$ at a volume fraction of 0.3. These plots are shown in Figure 16.

In Figure 16a, the x-displacement component FEA hollow and composite cylinder method results are observed to be in good agreement within the nanotube. However, as the midpoint between two neighboring nanotubes is approached (in the matrix), the results begin to slightly diverge. This same trend is observed in the normal total strain plot in Figure 16b. Volume averaged values of these field quantities will lead to differences in the components used to calculate both axial and transverse CTE as seen in Eqn. 2.14. The other total

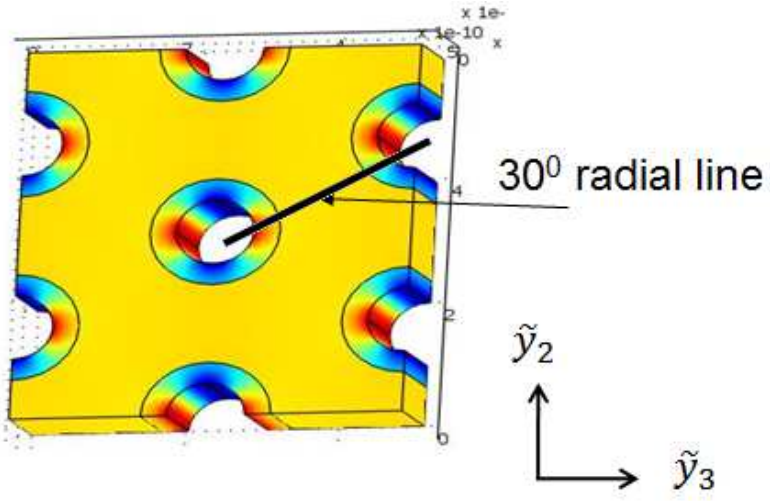

Figure 15: 30°radial line between center of nanotubes for plotting displacements, stresses, and strains.

strain components demonstrate a similar behavior. The total normal stress component shown in Figure 16c presents small differences between the FEA hollow and composites cylinder approaches. The differences occur in the nanotube region as opposed to the matrix region. Effective CTE results are observed to be more sensitive to the transverse components of stress than to any of the total strain components through subsitution of material properties into Eqn. 2.14. Therefore, the differences in CTE observed in Figure 14 are more directly driven by the differences shown in Figure 16c than in Figure 16b.

Another small source of error is observed by looking at the geometry of the hollow FEA representations in Figure 5. Nearest neighbor nantoubes are connected along lines 30° above the x-axis as shown in the line plots in Figure 16. However, at 0° relative to the x-axis, the distance between nearest neighbor nanotube centers (i.e. second nearest neighbors) is more than double the original distance. This difference in geometry representation will lead to different stress and strain plots between the FEA models and the composite cylinder model along such lines. These differences in the volume averaged stress and strain will thus lead to differences in the effective CTE components. The periodic hexagonal array RVE is an approximate cylindrically transversely isotropic representation of well-dispersed CNTS, and the CCM and Mori-Tanaka

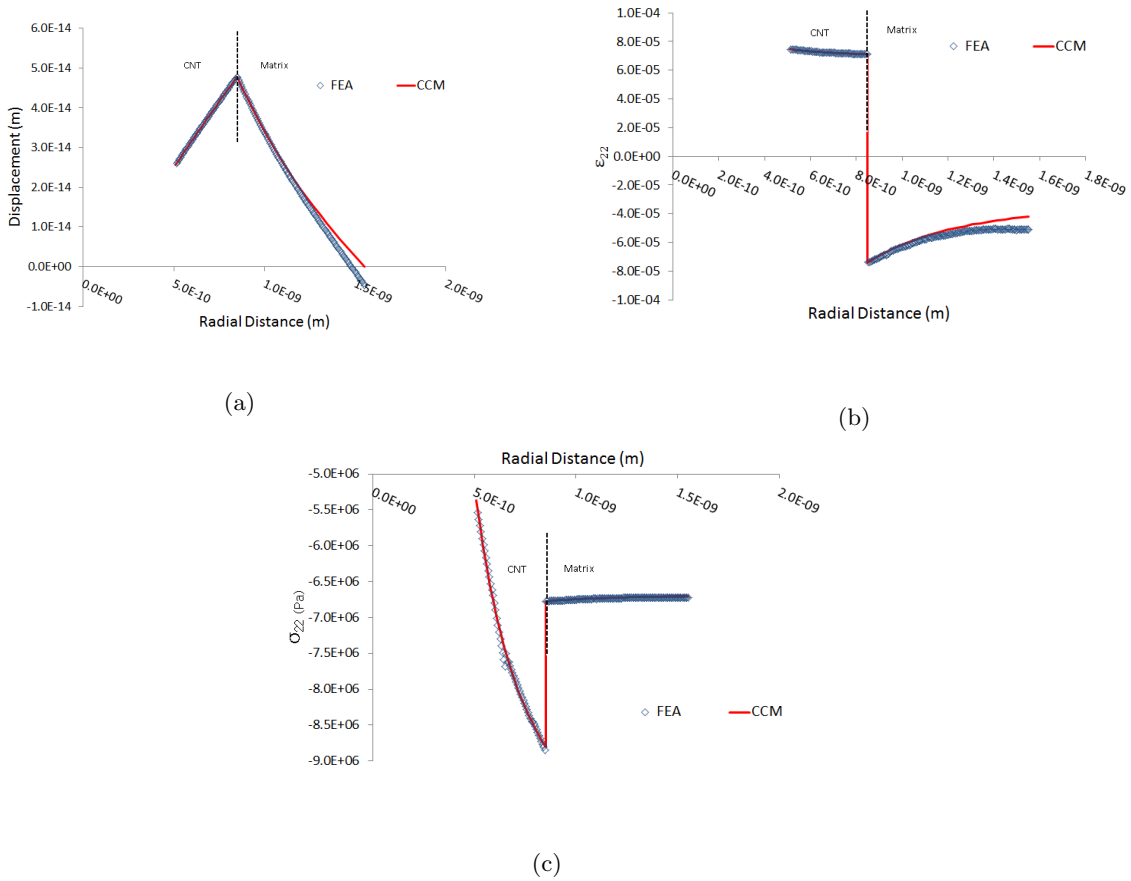

Figure 16: Comparison of the displacement, strain, and stress along a radial line of 30° for the hollow finite element and composite cylinders method results at a volume fraction of 0.3 and a ΔT of $10°K$.

models are explicitly transversely isotropic.

3.2 Interphase Effects on Effective Coefficient of Thermal Expansion Calculations

A 0.34 nm thick interphase region is added to the nanocomposite RVE in order to assess its influence on the effective axial and transverse CTE components[4]. The interphase elastic and thermoelastic properties

[4]The value for interphase thickness is selected to be consistent with previous studies [5] which has selected the value based on TEM images of nanotube pull-out from a polymer matrix.

are varied in three cases: i) an increase in elastic stiffness by a factor of 10 relative to the matrix stiffness (labeled 10E), ii) an increase in CTE of a factor of 10 relative to the matrix CTE (labeled 10a), and iii) an increase of both by a factor of 10 in stiffness and in CTE relative to the matrix (labeled 10Ea). Note that the inclusion of an interphase region leads to what is an interphase percolation as the volume fraction is increased to the interphase percolation volume fraction. This is the volume fraction at which the interphase regions of neighboring nanotubes comes into contact and begin to overlap. The composite cylinder method cannot be used in this overlap region as the interphase layer is no longer circular. The Mori-Tanaka model can also not be used as the inclusions are not ellipsoidal. As the volume fraction is further increased, the 3-phase (nanotube, interphase, matrix) RVE transitions to a 2-phase (nanotube, interphase) RVE where the composite cylinders method can again be used.

Results are produced for axial and transverse CTE using both a composite cylinder and FEA approach, with the 3-phase to 2-phase transition region associated with interphase percolation clearly identified, and are compared with the no-interphase composite cylinder method results as seen in Figure 17 and Figure 18.

There it is again observed for all three interphase cases and for both effective axial and transverse CTEs that the FEA hollow and composite cylinder method yield nearly identical results. For the effective axial CTE (Figure 17), all three interphase cases demonstrate a similar trend: a sharp decay prior to the interphase percolation, followed by a nearly linear decrease post interphase percolation. However, their behavior relative to the no-interphase case differ. For the 10E and 10a cases an increase of 100% relative to the no-interphase case is observed for the axial CTE at a volume fraction of 0.4, while at the same volume fraction, a much larger increase of 1300% is observed. These results indicate the strong interactions between elastic and thermoelastic properties which can lead to large increases in stress, and hence, in effective axial CTE, particularly when both properties are increased[5]. Based on observations from the no-interphase case, it is expected that the effective axial CTE of the nanocomposite should be dominated by the nanotube axial CTE. This is in fact the case for the 10E and 10a interphase cases as the effective axial CTE is much closer to

[5]A stiffer material may be more likely to have a lower CTE than a higher one, and vice versa.

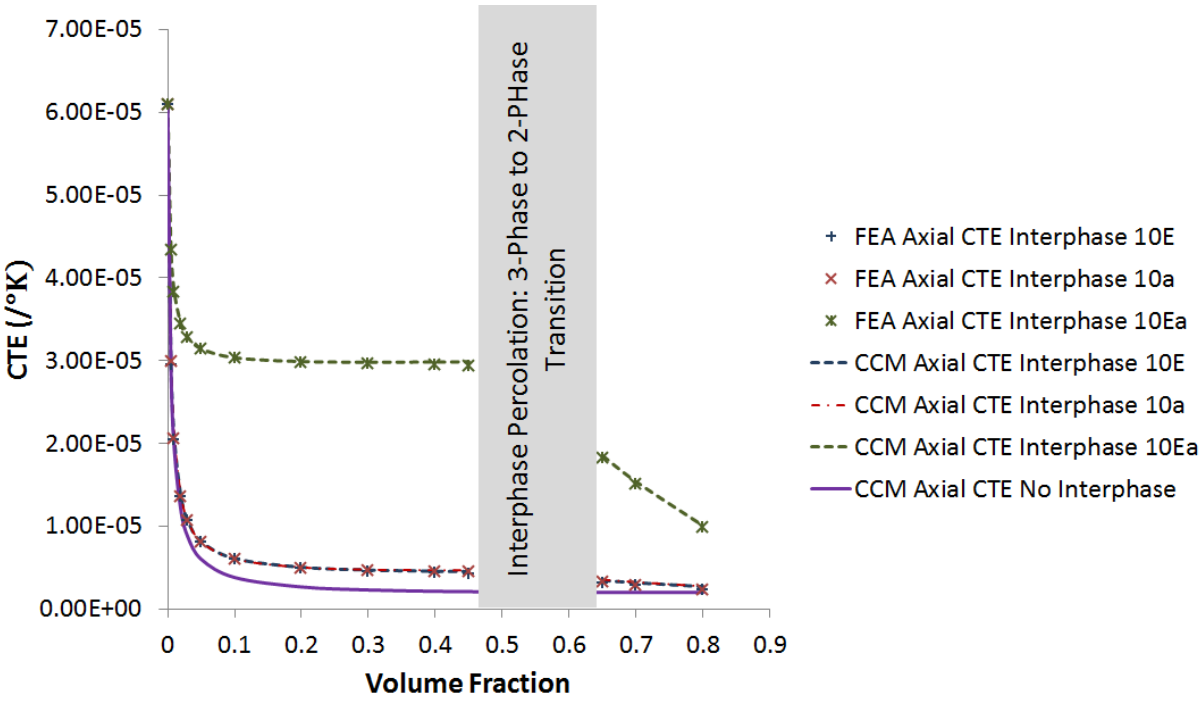

Figure 17: Comparison of the effects of interphase elastic properties and CTE on the effective axial CTE of the nanocomposite for an interphase thickness of 0.34nm.

the nanotube value than to either the matrix or interphase values. However, for the 10Ea case, the effective axial CTE is an order of magnitude larger than the axial CTE of the nanotube (i.e., it is on the order of the matrix value), indicating that the interphase region has become a significant influence on the effective axial CTE which is more than just a summation of the individual effects of identical increases in elastic and thermoelastic properties.

The transverse CTE results for the three interphase cases in Figure 18 demonstrate a sharply different behavior than was observed in the axial CTE case. There, the 10E case is observed to behave very similar to the no-interphase case, beginning with an initial increasing region, before following a decreasing trend with increasing volume fraction, maintaining relatively good agreement even in the post interphase percolation region. At a volume fraction of 0.4, the percent difference of the 10E case transverse CTE relative to that of the no-interphase case is 1%. In contrast, the 10a and 10Ea cases demonstrate a sharp, nearly linear increase

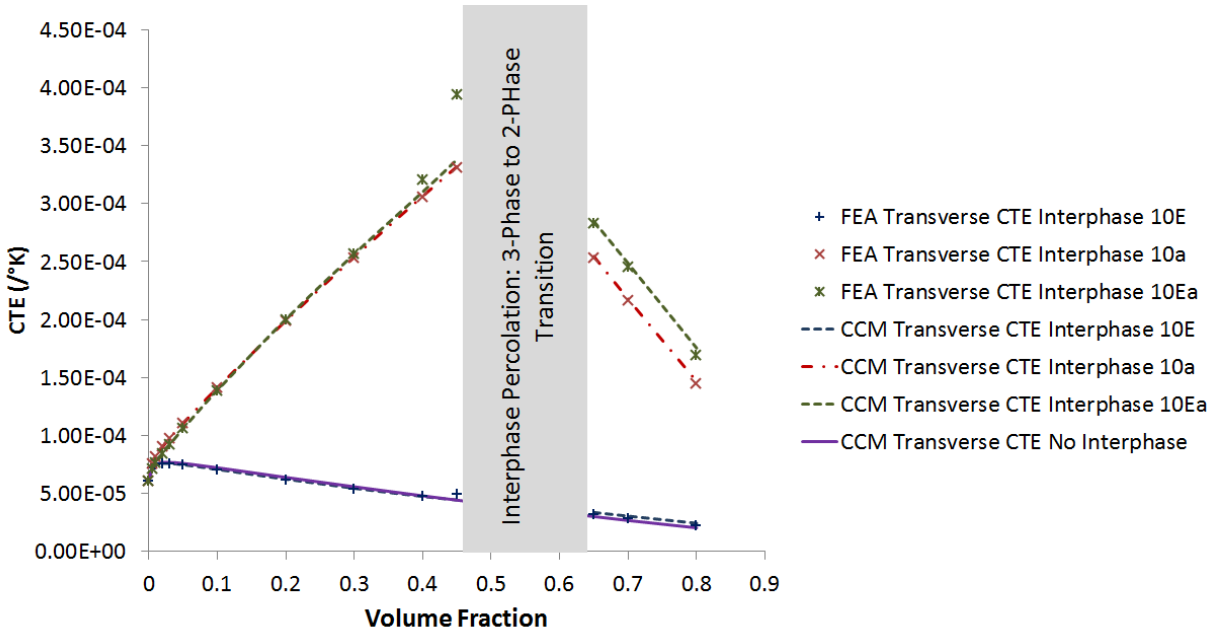

Figure 18: Comparison of the effects of interphase elastic properties and CTE on the effective transverse CTE of the nanocomposite for an interphase thickness of 0.34nm.

in transverse CTE with increasing volume fraction up until the interphase percolation volume fraction, and subsequently demonstrate a linearly decreasing behavior in the post interphase percolation region. In fact, prior to interphase percolation, both the 10a and 10Ea cases yield approximately the same transverse CTE, on the order of a 550% increase relative to the no-interphase case at volume fraction of 0.4, with the only differences between the two cases being observed in the post interphase percolation region where the 10Ea case demonstrates a significantly larger transverse CTE value than the 10a case. As the results for the no-interphase case indicated that the transverse CTE was a matrix dominated property, the relatively small effect of the 10E interphase on the effective transverse CTE is not surprising as the matrix and interphase have the CTE. However, when the interphase CTE is increased, the effective transverse CTE demonstrates an interphase dominated response, with both the 10a and 10Ea cases yielding values on the order of the interphase CTE. Effective transverse properties being greatly affected by increases in interphase properties has also been observed for the effective elastic properties [5], and therefore indicates that the effective CTE

response follows expected trends. The question which remains is why there were no combined effects of increasing stiffness and CTE in the effective transverse CTE as were observed in the effective axial CTE.

To better understand how the effective CTE components are affected by the interphase layer, the transverse (x-direction) normal total strain, transverse (x-direction) normal stress, and axial (z-direction) normal stress[6] are observed in Figure 19 for all three interphase cases. The normalized total normal strain is observed to increase by a factor of 10 relative to the no-interphase case in both the interphase region and in the matrix for the 10E case. In the interphase region, both the 10a and 10Ea cases increase by a factor of 50, while in the matrix, the 10a case increases by a factor of 50 and the 10Ea by a factor of 100. In terms of the transverse normal stress, the 10E case demonstrates at most a factor of 2 increase in the interphase region, while the 10a case demonstrates on average a factor of 4 increase. In contrast, the 10Ea case not only shows larger increases (factors of 10 and 6 in the interphase and matrix, respectively), but also demonstrates a change in sign of the transverse stress in the nanotube from compression to tension. The axial normal stress in the nanotube and matrix for all three interphase cases is increased by less than a factor of two. The same is true for the axial normal stress in the interphase region for cases 10E and 10a, however, for case 10Ea, axial normal stress increases by a factor of 14.

These regional variances in the total strain and stress will significantly affect the volume averages, and therefore the effective CTE components of the nanocomposite. In particular, the factor of 14 increase in the axial stress of the 10Ea case is the direct cause of the large increase in effective axial CTE observed in Figures 17 and 18. While the transverse normal stress and transverse total normal strain exhibit increases of similar scale and larger, both of these volume averaged components are marginalized in calculating the effective axial CTE due to multiplication with the Poisson's ratio as seen in Eqn. 2.14 which effectively reduces their contributions by a factor of 10. For the effective transverse CTE, it is the increases observed in the transverse normal stress which lead to the behaviors observed for the three interphase cases. In looking at effective transverse CTE in Eqn. 2.14, it is observed that the axial normal stress is multiplied by κ_{23}^{eff}

[6]The axial total normal strain is identically zero in all phases.

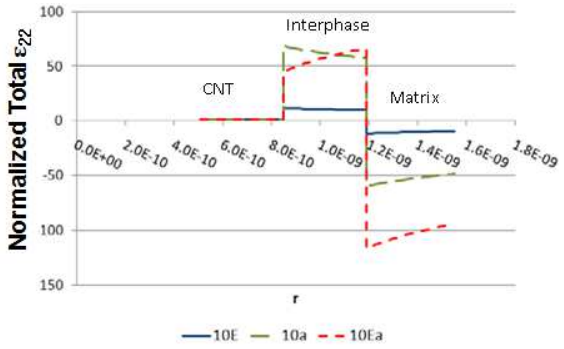

(a) Normalized x-Direction Normal Total Strain

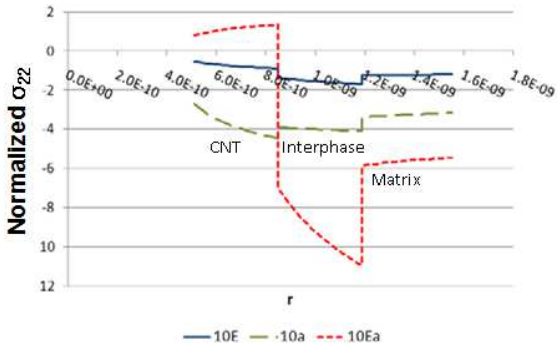

(b) Normalized x-Direction Normal Stress

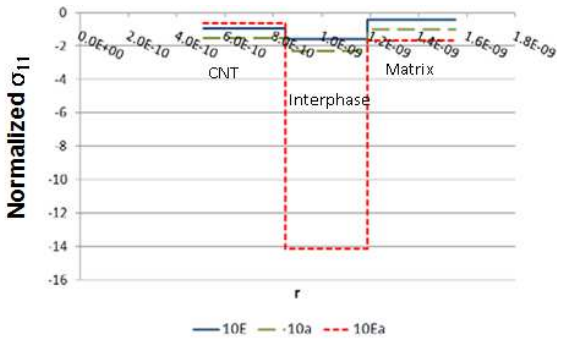

(c) Normalized x-Direction Normal Stress

Figure 19: Comparison of the normalized strain and stress along a radial line 30° for the composite cylinders method results at a volume fraction of 0.3 for all three interphase cases.

while the transverse normal stress is multiplied by the much larger E_{11}^{eff}. Though the transverse total normal strains are multiplied by both quantities, the strain values are so small that they remain overshadowed by the stress contributions, and more specifically the transverse normal stress. That the 10a and 10Ea effective transverse CTEs demonstrate similar behavior in Figures 17 and 18 despite the 10Ea case having a much larger increase in the interphase transverse normal stress can be understood in terms of the contribution of the nanotube transverse normal stress for the 10Ea case having changed sign from compression to tension, and therefore reducing the overall volume averaged stress. Thus, it is the interphase and impact of the interphase on neighboring layers which can have substantial impact on the effective CTE of the nanocomposite both before and after interphase percolation. This is in contrast to previous observations regarding the elastic,

thermal, and electrical properties where it was observed that the interphase had limited impact on the effective properties until after interphase percolation[5, 35, 10].

3.3 Well-Dispersed, Randomly Oriented Nanotubes

The effects of randomly oriented fibers is analyzed using the Mori-Tanaka method. The CCM model cannot account for random orientation, and the FEA model would be too computationally expensive to account for random orientation. The FEA RVE would require many different orientations in order to be a good representation of random orientation, and thus it would become to large to calculate the displacement field efficiently. The effective nanotube and nanotube with interphase properties for all three interphase cases are used to obtain local nanoscale RVE stress concentration tensors based on Eqn. 2.27 and to subsequently obtain the effective CTE for nanocomposites consisting of randomly oriented nanotubes through application of Eqn. 2.29. The effective CTEs for the no interphase case and the three interphase cases are provided in Figure 20 along with the axial and transverse CTE for the no-interphase case previously provided. There the no-interphase case effective CTE for the randomly oriented nanotube nanocomposite is observed to lie between the axial and transverse CTE results for the aligned nanotube nanocomposite, having a less sharply decreasing trend as compared to the axial CTE results. This seems to indicate that the randomly oriented results will closely reflect the axial CTE results. However, while the randomly oriented results for the 10E interphase case do only slightly increase relative to the no-interphase case as was likewise observed for the 10E axial CTE, the 10a randomly oriented CTE does not lie atop the 10E results as it did in the axial CTE results. Instead, the 10a randomly oriented results are significantly increased relative to the 10E randomly oriented results indicating that the large increases observed in the transverse CTE for the 10a case do have a significant effect on the effective CTE. However the relative scale of impact of the axial and transverse CTE results is illustrated in the 10Ea results for effective CTE. Despite the 10a and 10Ea having the same large increases in effective transverse CTE, it is the large increase in effective axial CTE of the 10Ea case relative to the 10a case which leads to the exceptionally large increase in effective CTE for the randomly

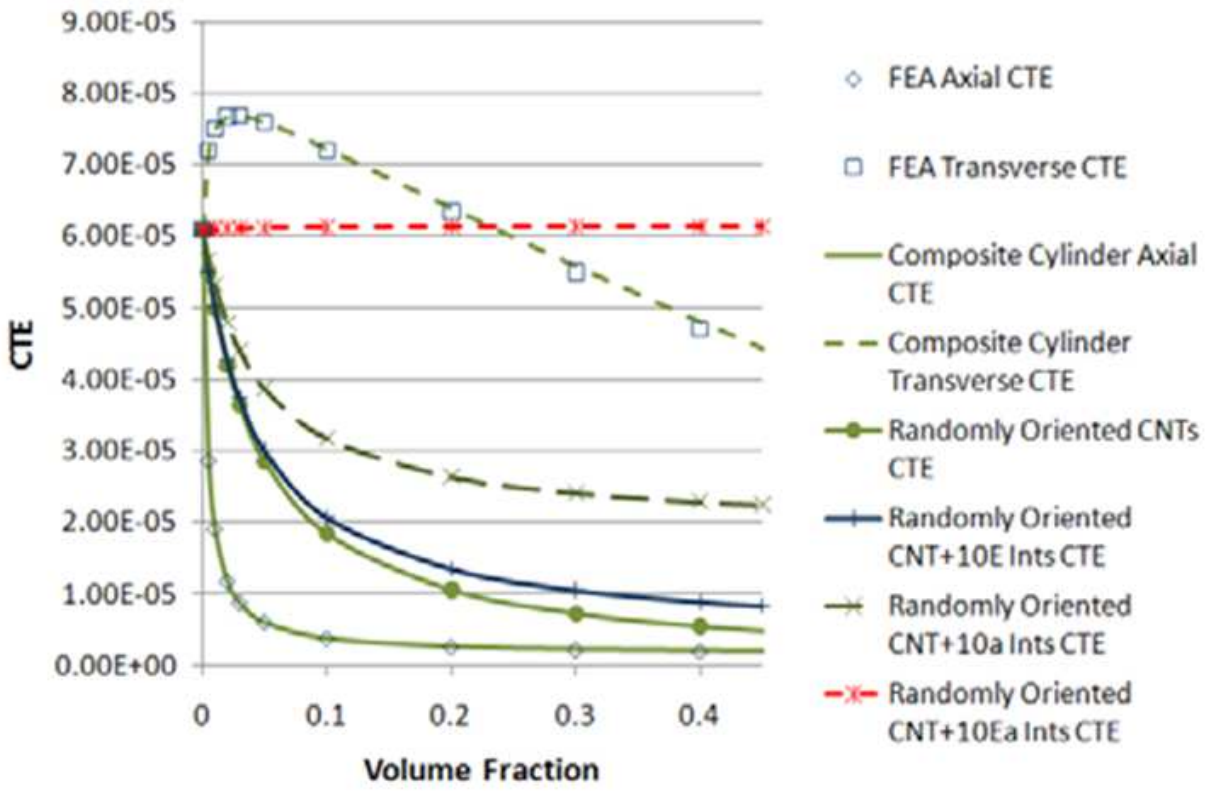

Figure 20: Comparison of the effects of interphase elastic properties and CTE on the effective transverse CTE of the nanocomposite for an interphase thickness of 0.34nm.

oriented nanotube nanocomposite. The combination of axial and transverse properties of nanotubes was likewise observed to govern effective elastic, thermal and electrical properties of randomly oriented nanotube nanocomposites, with the larger contributor again being the axial properties of the nanotube and interphase.

3.4 Clustered, Aligned Nanotubes with No Interphase Layer

Effective axial and transverse CTE results for clustered, aligned nanotubes with no interphase layers are produced using both an FEA method and the hybrid analytical and computational method described in Section 2.7. Note that the mechanical properties needed to solve for effective CTE in Eqn. 2.14 are determined

from the applied periodic boundary conditions. The results for effective clustered CTE using the FEA method compared with the no clustering cases is seen in Figure 21. Note that data for Cluster 1, Cluster 2, Cluster

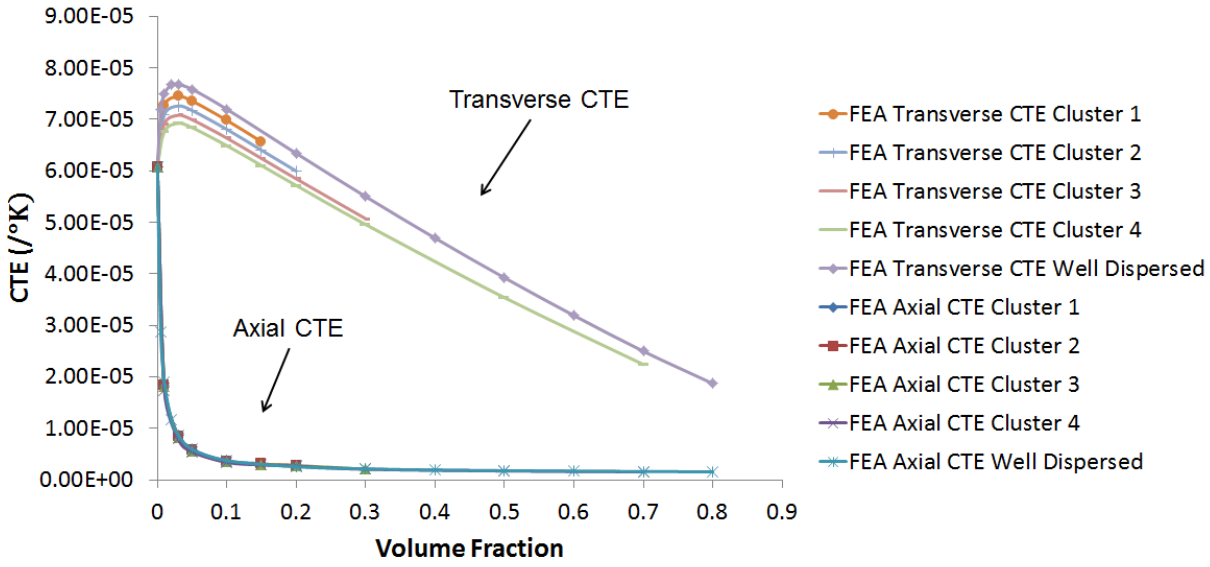

Figure 21: Effective clustered axial and transverse CTE calculated using FEA method and comparison with the no clustering cases.

3, and Cluster 4 are available for volume fractions up to $V_f = 0.15$, $V_f = 0.23$, $V_f = 0.38$, and $V_f = 0.75$ respectively. The position of the nanotubes is fixed in each clustered step configuration, so the packing fraction only increases with increasing cluster steps. The same trends seen in the no clustering cases for axial and transverse CTE are observed for each clustering step. The clustered axial CTE responses follow the same sharply decreasing trend towards the axial CNT coefficient of thermal expansion seen in the non-clustered cases. The maximum observed percent difference between all clustered axial CTE results and the non-clustered results is 4%. It is observed in Ref.[13] that axial mechanical properties are minimally impacted by clustering. For example, the axial Young's modulus, E_{11}, only varies by 0.1% due to clustering.

The clustered transverse CTE responses follow the same trend with the initial increase in effective CTE above the matrix value of CTE as seen in the non-clustered cases. However, it is also observed that each additional

level of clustering decreases the effective transverse CTE. Cluster 4 has an average percent difference of 10% as compared to the non-clustered case. It is shown in Ref. [13] that clustering leads to small increases in transverse modulus (E_{22}) and shear modulus (G_{23}) on the order of 2.3%. It is believed that these small increases in transverse mechanical properties are responsible for the small decreases observed in the clustered transverse CTE results. The stiffer transverse properties would resist thermal expansion, and could thus lead to marginal decreases in effective transverse CTE.

Effective axial and transverse CTE are also calculated using the hybrid analytical and computational technique. These results are provided in Figure 22. The axial CTE is shown to be minimally impacted by clustering steps as the same sharply decreasing function is observed. However, the effective transverse CTE shows a significant difference for the clustered steps versus the well dispersed case. There is no initial increase in CTE above the matrix CTE value, and the values are much lower than the well dispersed case. Using this hybrid approach to inversely solve for Eshelby tensors for each phase may not be capturing the true interaction between neighboring nanotubes. This type of inverse approach also does not represent a physical quantity as Eshelby tensors are strictly dependent on inclusion shape and the matrix material parameters. This approach is still used in Section 3.5 to calculate effective CTE for clustered cases with interphase layers.

3.5 Clustered, Aligned Nanotubes, with Interphase Layers

The hybrid analytical and computational method outlined in Section 2.7 is used to calculate effective CTE for clustered, aligned nanotubes with interphase layers. This method has the potential to be used to predict effective properties for randomly oriented bundles for clustering and clustering with interphase RVEs. The same parametric study of three different types of interphase layers given in Section 2.4 is used to assess the combined effects of clustering and interphase layers on effective nanocomposite CTE. The results for effective axial CTE for the four clustered steps with the 10E interphase layer are shown in Figure 23 compared with the interphase case without clustering. It is again noted that Cluster 1, Cluster 2, Cluster 3, and Cluster 4 can only be analyzed up to maximum volume fractions of $V_f = 0.15$, $V_f = 0.23$, $V_f = 0.38$, and $V_f = 0.78$

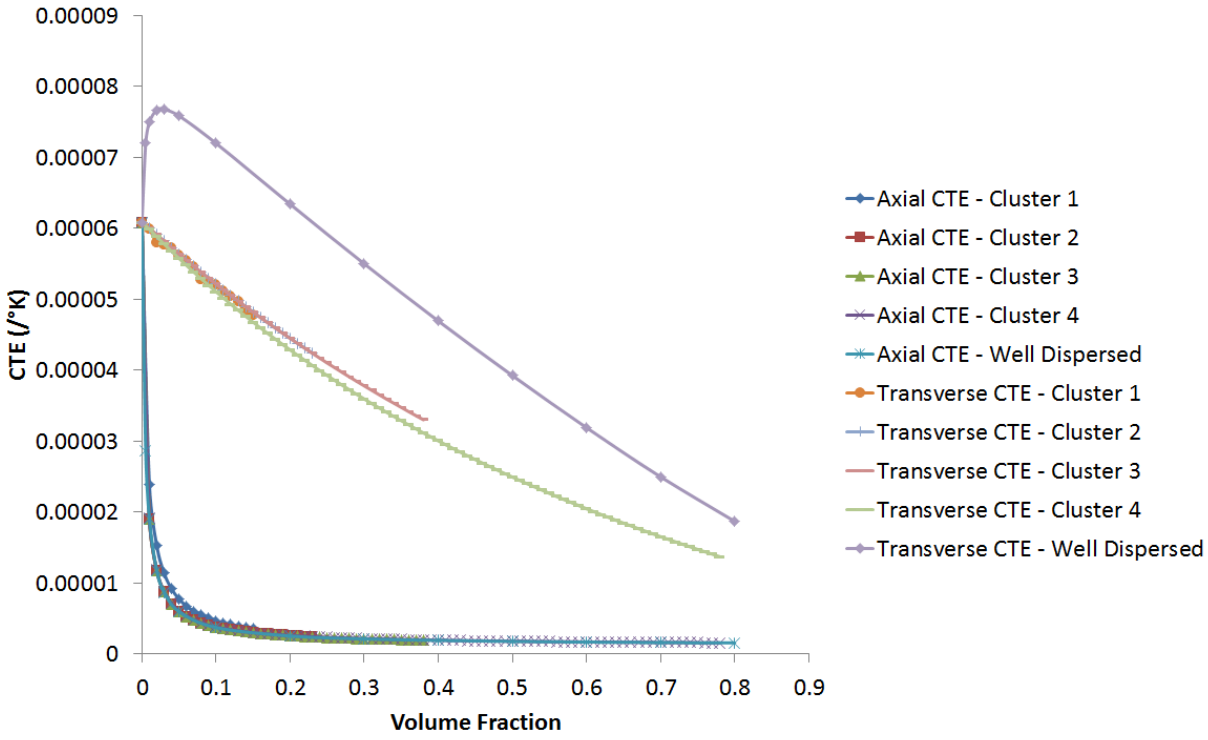

Figure 22: Effective axial and transverse CTE calculated using the hybrid analytical and computational technique and comparison with the no clustering CCM cases.

for the clustered with interphase cases due to the packing fraction of the nanotubes at each clustering step. The sharp decay trend is again seen for all four clustering steps. This seems to indicate that clustering only has a marginal impact on the effective axial CTE for the 10E interphase case. There is some variability between the clustered arrangements at volume fractions near $V_f = 0.1$. The source of these differences could be attributed to the inverse method that is used to solve for effective Eshelby tensors for each phase. Since Eshelby tensors are based on geometry and material parameters, inversely solving for Eshelby tenors does not have a phyiscal relation. Approximating these Eshelby tensors in this way could lead to the small differences in axial CTE seen in Figure 23.

The results for the effective transverse CTE for the four clustered steps with the 10E interphase layer are shown in Figure 24 compared with the interphase case without clustering. The transverse CTE values

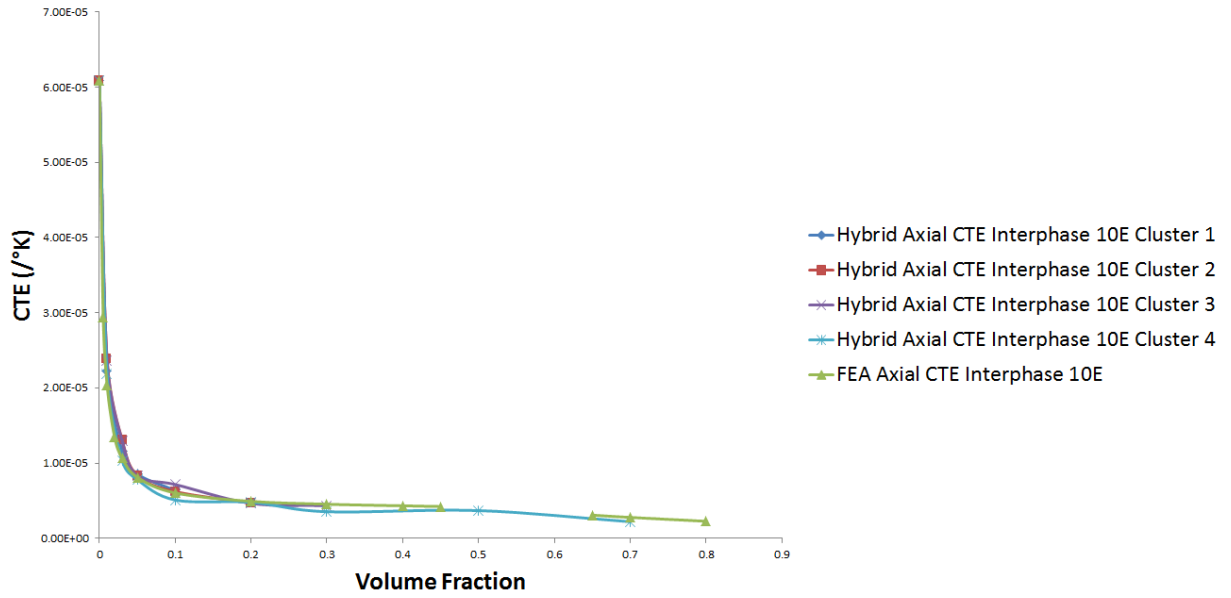

Figure 23: Effective axial CTE for clustering with a 10E interphase layer and comparison with the no clustering 10E interphase layer case.

are shown to decrease with increasing clustering levels. It is shown in Ref. [13] that clustering and a 10E interphase layer have a large combined effect on the effective transverse modulus, E_{22}, and the two shear moduli, G_{12} and G_{23}. E_{22} is shown to have an average increase on the order of 19.49% and G_{12} and G_{23} are shown to have an average increase on the order of 19.95% and 14.2% respectively. It is thought that the increase in these mechanical properties, specifically E_{22} and G_{23}, due to clustering and the 10E interphase layer play a role in the decreasing of the transverse thermal expansion coefficient with increasing cluster degree. A larger effective stiffness would resist displacements due to thermal loads. Effective mechanical properties have already been shown to affect CTE as seen in Eqn. 2.14 due to the coupled mechanical and thermal response.

The results for the effective transverse CTE for the four clustered steps with the 10a interphase layer are shown in Figure 25 compared with the interphase case without clustering. Again, the exponential decrease in axial CTE is seen for all four clustering steps, and this compares well with the no clustering with interphase

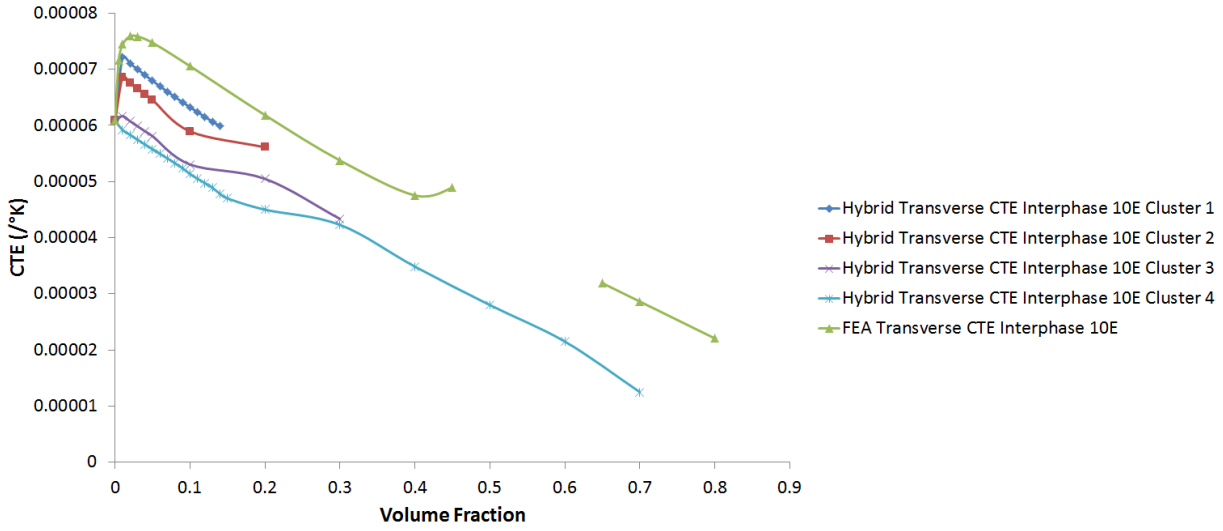

Figure 24: Effective transverse CTE for clustering with a 10E interphase layer and comparison with the no clustering 10E interphase layer case.

layer case. It is again believed that the inverse Eshelby solution method leads to the small observable differences in axial CTE. This response suggests that clustering has a marginal impact on the effective axial CTE for the 10a interphase case.

The results for the effective transverse CTE for the four clustered steps with the 10a interphase layer are shown in Figure 26 compared with the interphase case without clustering. The four clustering steps are shown to be in good agreement with each other and in relatively good agreement with the no clustering with 10a interphase layer case. After a volume fraction of $V_F = 0.55$, it seems that the transverse CTE response for clustering with 10a interphase layer is dominated by the nanotube value of CTE. As was shown in the no clustering with 10a interphase layer case, the value of transverse CTE quickly decreases towards the nanotube value after the percolation volume fraction is reached.

The results for the effective axial CTE for the four clustered steps with the 10Ea interphase layer are shown in Figure 27 compared with the interphase case without clustering. All four clustering steps are again shown to have very similar values of effective axial CTE. It is also again shown that clustering seems to play a

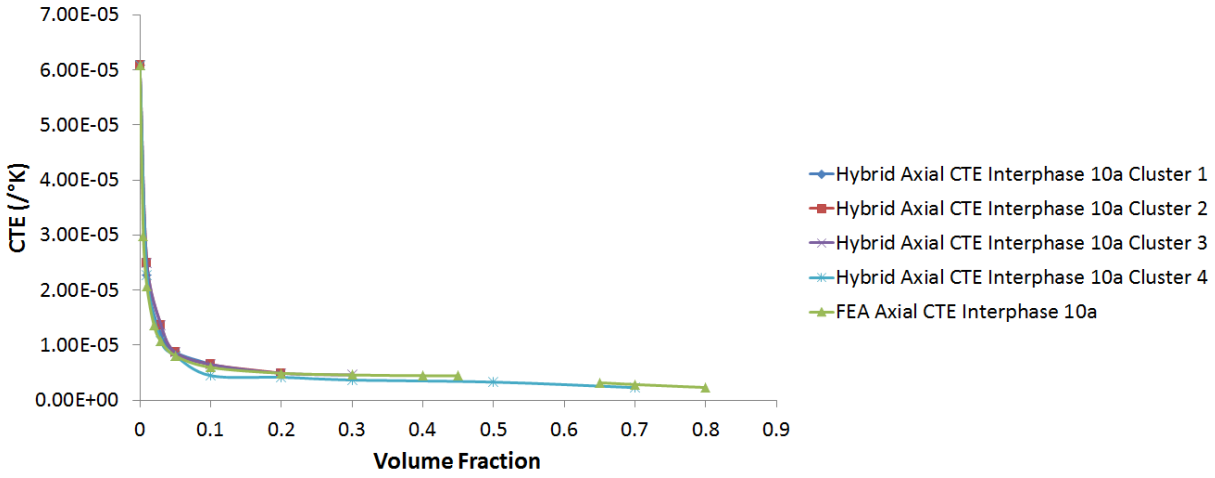

Figure 25: Effective axial CTE for clustering with a 10a interphase layer and comparison with the no clustering 10a interphase layer case.

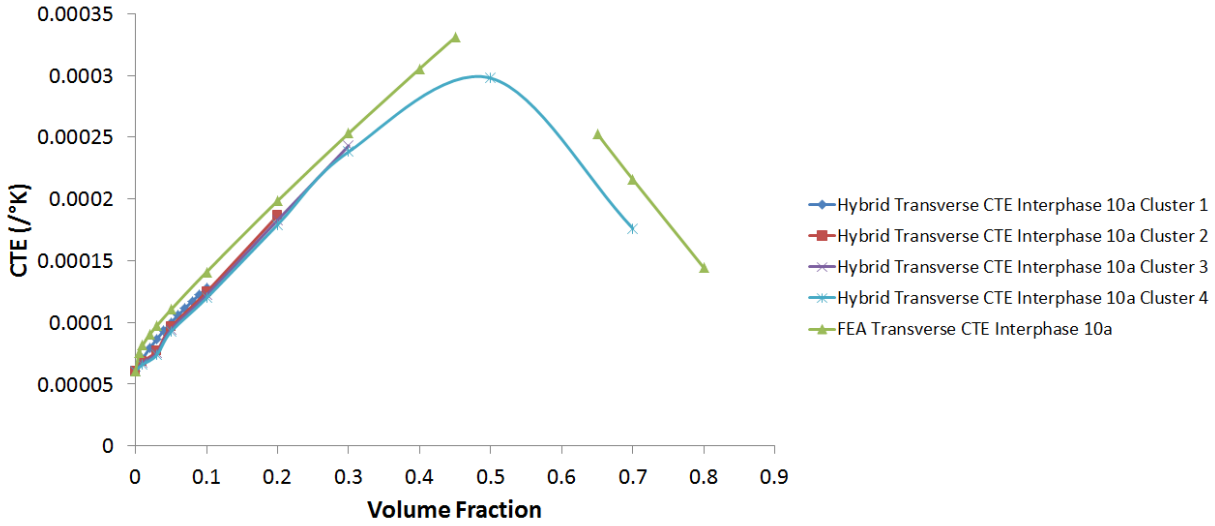

Figure 26: Effective transverse CTE for clustering with a 10a interphase layer and comparison with the no clustering 10a interphase layer case.

minimal role in predicting effective axial properties, even when combined with an interphase layer.

The results for the effective transverse CTE for the four clustered steps with the 10Ea interphase layer are

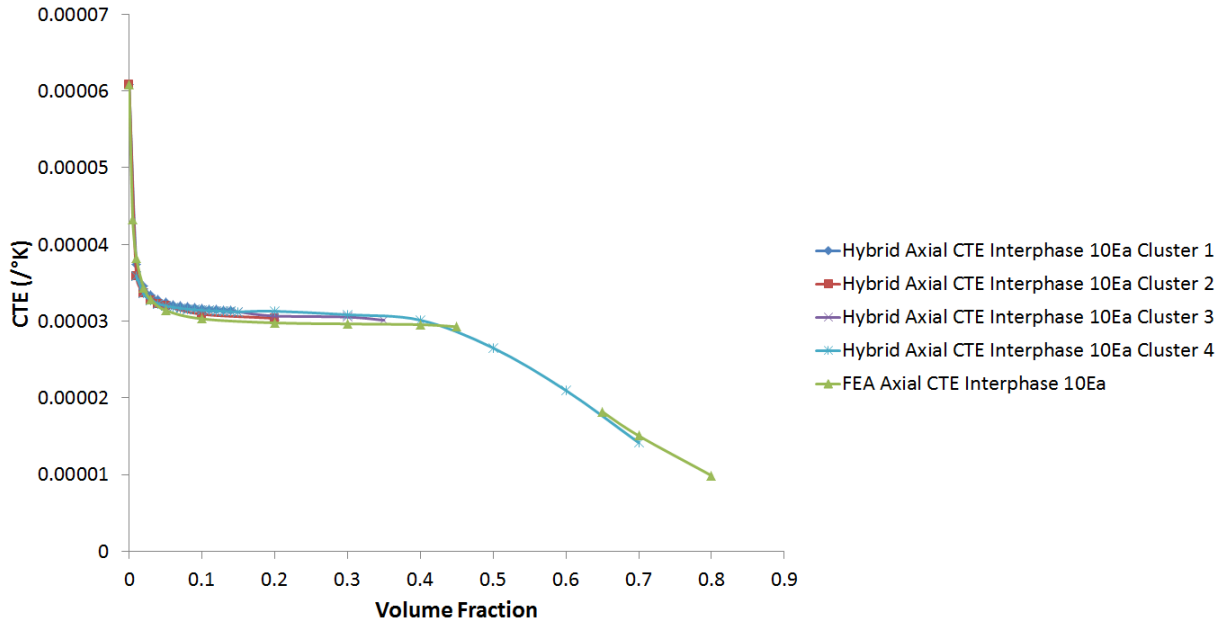

Figure 27: Effective axial CTE for clustering with a 10Ea interphase layer and comparison with the no clustering 10Ea interphase layer case.

shown in Figure 28 compared with the interphase case without clustering. The four clustering steps are shown to only differ slightly from each other. There is also relatively good agreement with the no clustering with 10a interphase region case. As is seen for the transverse CTE response for clustering with a 10a interphase layer, after a volume fraction of $V_F = 0.55$, it seems that the transverse CTE response for clustering with the 10Ea interphase layer is dominated by the nanotube value of CTE. As is shown in the no clustering with 10Ea interphase layer case, the value of transverse CTE quickly decreases towards the nanotube value after the percolation volume fraction is reached.

Axial CTE for clustering with interphase is compared with the no clustering with interphase in Figure 29. Note that only cluster level 4 is shown for the clustering results. Clustering is shown to have a minimal effect on the axial CTE for the interphase cases (about 1-2%).

Transverse CTE for clustering with interphase is compared with the no clustering with interphase in Fig-

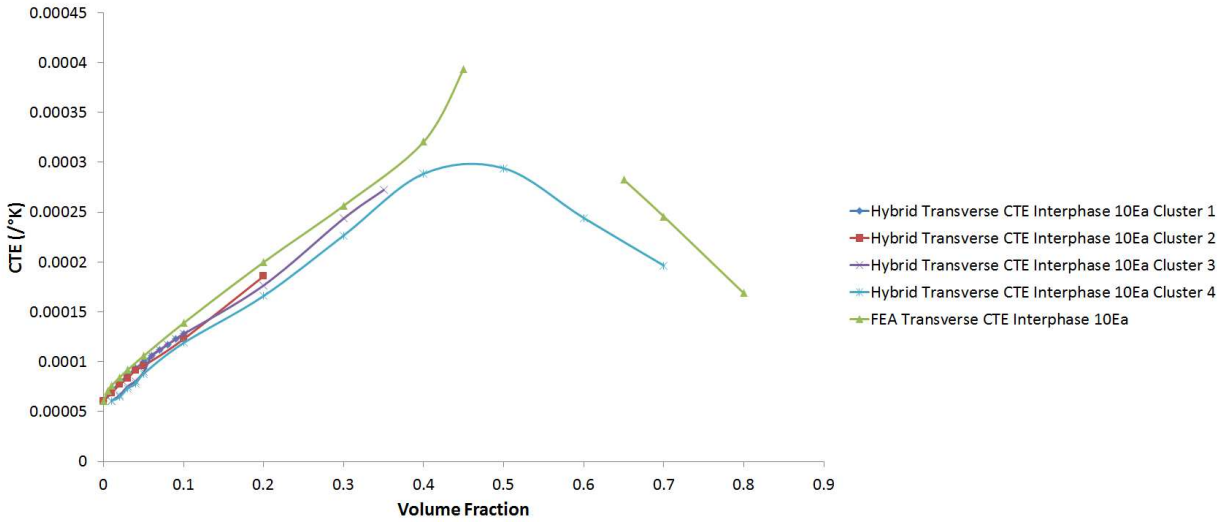

Figure 28: Effective transverse CTE for clustering with a 10Ea interphase layer and comparison with the no clustering 10Ea interphase layer case.

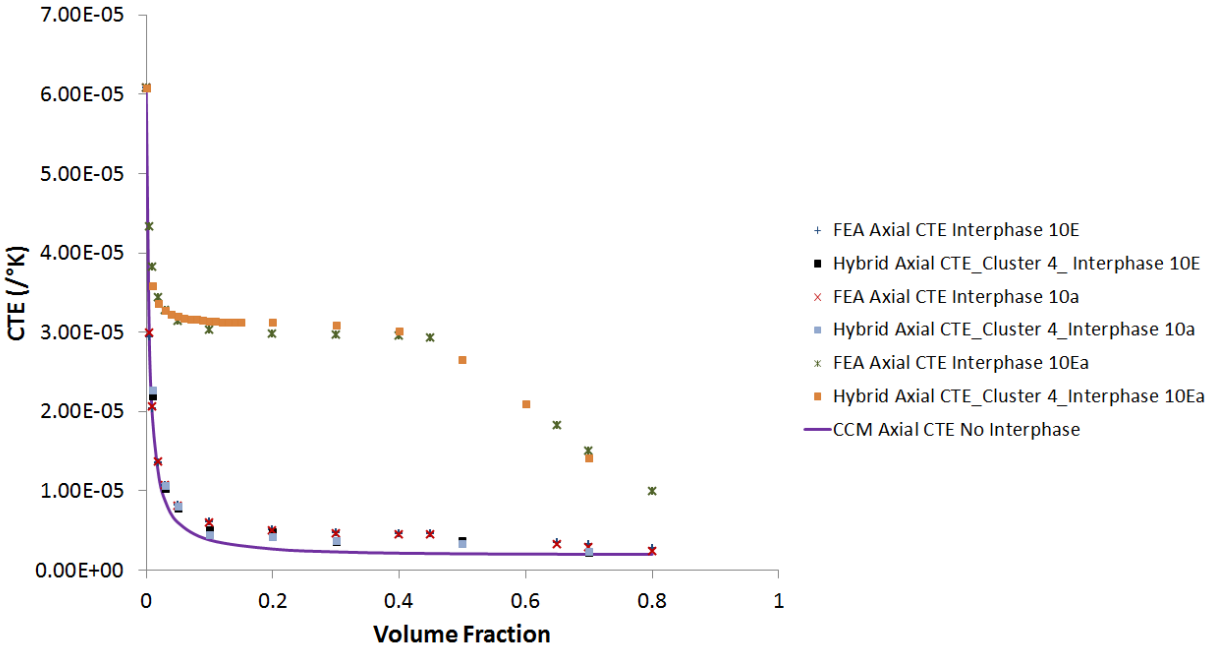

Figure 29: Effective axial CTE for clustering with interphase layers.

ure 30. Note that only cluster level 4 is shown for the clustering results. Clustering is shown to have a measurable effect on the transverse CTE for the interphase cases (between 15% and 30%). A summary of

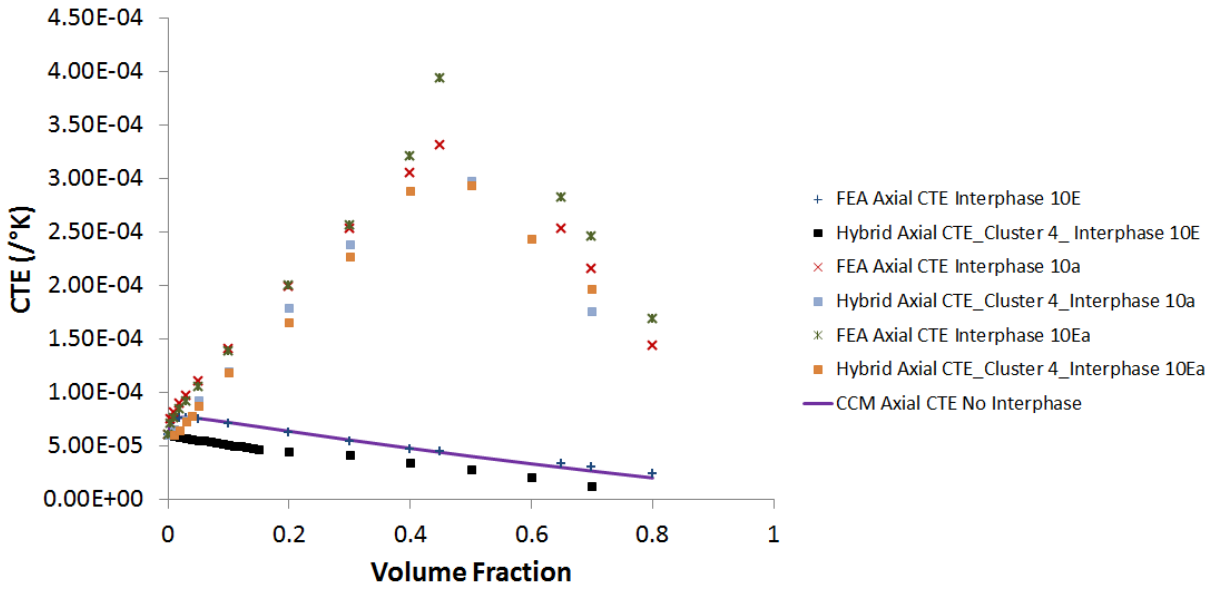

Figure 30: Effective transverse CTE for clustering with interphase layers.

the effects of clustering with interphase on effective CTE is seen in Table 2. The effecits of clustering for a few mechanical properties are also included from Ref. [34].

Table 2: Summary table of clustering and clustering with interphase effects on effective CTE.

	No Interphase Layer	10E Interphase Layer	10a Interphase Layer	10Ea Interphase Layer
Property	Variation with clustering (%)	Variation with clustering (%)	Variation with clustering (%)	Variation with clustering (%)
E_{11}	0.10	0.10	-	-
E_{22}	2.33	10.35	-	-
ν_{12}	0.96	1.87	-	-
ν_{23}	3.17	11.63	-	-
G_{12}	1.96	7.78	-	-
G_{23}	2.24	8.38	-	-
α_{11}	1.8	1.34	1.25	1.46
α_{22}	3.2-10.1	16.1-32.1	15	14.3

4 CTE Significance to Structural Health Monitoring

The significance of thermal expansion to structural health monitoring is demonstrated in this section through an example for a composite patch on a ship operating in different environmental conditions. The composite patch is assumed to have a carbon nanotube-epoxy nanocomposite piezoresistive sensor embedded in order to sense damage. The demonstration starts with Eqn. 2.4. The value chosen for effective CTE, $\boldsymbol{\alpha}^{\text{eff}}$, is for the well-dispersed, 10Ea interphase layer at a volume fraction of 0.4. The temperature difference is assumed to be 55K for a ship traveling from warm to cold waters. The thermal strain is calculated to be 0.0176 as seen in Eqn. 4.1.

$$^{\text{T}}\boldsymbol{\epsilon} = (3.2 * 10^{-4})(303K - 248K) = 0.0176 \tag{4.1}$$

A gauge factor based on this thermal strain is then determined by utilizing Figure 31 from Ref. [3].

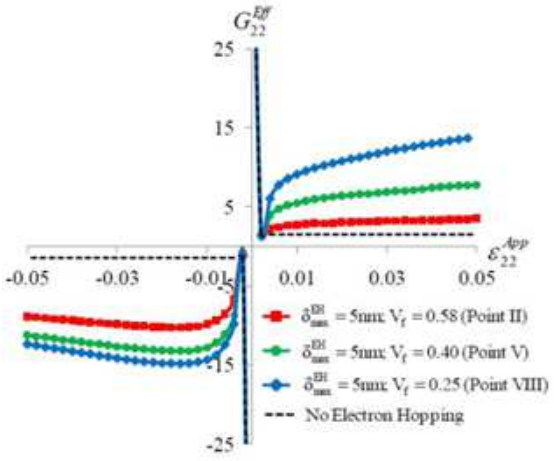

Figure 31: Effective macroscale gauge factors at different applied strains at multiple volume fractions [3].

The gauge factor for the thermal strain is therefore $^{\text{T}}G = 5.5$. The fractional change in resistance is then calculated to be $^{\text{T}}\left[\frac{\Delta R}{R}\right] = 0.0968$ by way of Eqn. 4.2

$$G = \frac{\frac{\Delta R}{R}}{\epsilon} \tag{4.2}$$

A total strain is assumed to be $^{\text{Tot}}\boldsymbol{\epsilon} = 0.02$. Referencing Figure 31, the total gauge factor is $^{\text{Tot}}G = 5.75$.

Eqn. 4.2 is used to get a total fractional change in resistance of ${}^{\text{Tot}}\left[\frac{\Delta R}{R}\right] = 0.115$. Therefore, the thermal contribution to this total fractional change in resistance is 84%. It is clear how important the effects of effective CTE are on calibrating a piezoresistive sensor. In this assumed condition, thermal expansion accounts for a majority of the sensed fractional change in resistance. It is therefore necessary to calibrate a piezoresistive sensor for thermal loads if a mechanical structural health monitor is desired.

Another example is demonstrated by assuming a total strain of ${}^{\text{Tot}}\boldsymbol{\epsilon} = 0.1$. The total gauge factor for this strain is ${}^{\text{Tot}}G = 7.5$. Eqn. 4.2 is used to get a total fractional change in resistance of ${}^{\text{Tot}}\left[\frac{\Delta R}{R}\right] = 0.75$. The thermal contribution is now 13%, showing that thermal expansion effects are important even at higher total strains.

5 Conclusions

Several analytical and computational micromechanics techniques are presented for determining the effective coefficient of thermal expansion of carbon nanotube-epoxy nanocomposites. The composite cylinders method is used to calculate effective CTE for well-dispersed, aligned nanocomposites with and without interphase layers. This modeling method is used as it allows for analytical modeling of hollow fibers and interphase layers are easily added as additional layers in the composite cylinder assemblage. A finite element model consisting of a solid and a hollow configuration is utilized to determine effective CTE for these same aligned nanocomposites. The FEA model allows for modeling of more complex geometries, and verification of the model with the CCM model gives confidence that this FEA model can be utilized for more complicated cases. The FEA hollow configuration is also used to determine CTE for aligned cases with interphase layers and clustering cases. The solid FEA case is done to show that an effective fiber is a good approximation of the hollow fiber, especially at low volume fractions. This solid fiber RVE also allows for direct comparison with the Mor-Tanaka method used to account for random orientation. The Mori-Tanaka method is used to compute CTE for aligned, no interphase cases and the randomly oriented cases with and without interphase layers. A hybrid analytical and computational model using the Mori-Tanaka method and FEA is used to calculate effective CTE for the clustered and clustered with interphase cases. The hybrid model will allow for future modeling of random orientation for clustering and clustering with interphase cases.

For both the axial and transverse CTE of aligned nanotube nanocomposites with and without interphase regions, the computational and analytic micromechanics techniques are shown to give similar results. In terms of specific contributions of the interphase regions to the effective CTE components, it is observed that increases in interphase CTE, and even more so, increases in interphase CTE accompanied with increases in interphase stiffness, could yield significant impact on the effective axial and transverse CTEs, even prior to interphase percolation volume fractions.

The effective axial and transverse CTEs of the nanotubes with and without interphase are used to determine

local nanoscale RVE stress concentration tensors, which in turn are used to obtain the effective CTE for nanocomposites consisting of randomly oriented nanotubes both with and without interphase regions. The effective CTE for the randomly oriented nanotube nanocomposites are observed to be influenced by the factors influencing both the axial and transverse CTEs in the aligned nanotube nanocomposite cases, but are more susceptible to influences on the axial CTE than on the transverse, and are thus similarly affected by the interphase region properties. The randomly oriented nanotube nanocomposite CTE results are amenable to comparison with experimental data, and are presently being compared against experimental data in the literature for well characterized single-wall carbon nanotube nanocomposite systems.

The effective axial CTE is shown to not be significantly affected by different levels of clustering in both the FEA analysis and in the hybrid analytical and computational technique. The effective transverse CTE is shown to decrease with increasing clustering steps in the FEA analysis. However, the hybrid technique did not demonstrate this trend. The addition of an interphase region to the clustered configurations is shown to have a combined effect for all three interphase cases.

It is shown in Section 4 that CTE plays an important role in the calibration of a piezoresistive deformation sensor. Therefore, thorough quantification of the thermal expansion response of the nanocomposite material described in this work is necessary if a structural health monitoring sensor is desired. This work provides important information in regards to the thermal expansion response, and future work will continue into damage modeling of this material system. The thesis work made an important step in the right direction towards a structural health monitoring sensor for composite patches and other applications.

6 Future Challenges

Future work looks to add CTE response into a structural health monitoring sensor for composite patch applications. This will require more research into damage modeling of the carbon nanocomposite epoxy material system, and this will require more advanced modeling techniques (such as cohesive zone damage modeling).

This thesis work was completed with the aim of providing utility to the Naval Engineering community at large. The Navy is currently addressing problems associated with thermal expansion of ship flight decks. The Naval Surface Warfare Center Carderock Division (NSWCCD) has been tasked with modeling the thermal impact due to vertical take off craft, such as the Osprey. These craft exert large thermal loads during operation, and the flight decks are believed to have suffered measurable damage. It is not yet known if this problem will require a material system solution, but it is imperative that the Navy be able to model and predict failure of these flight decks. In order to model this damage, details about the thermal response of a material system should be quantified. Again, it is possible that cohesive zone damage modeling could be beneficial to address this modeling necessity.

Carderock is also involved in modeling a metal matrix nanocomposite material system called covetics. This material contains many different phases of nanocarbon, as shown in Figure 32, and predicting effective properties will require a comprehensive multiscale model. Carderock is interested in models that predict these effective properties and damage evolution of this new materials system. Preliminary experimental tests have shown high thermal conductivity for copper covetics and high electrical conductitiy for aluminum covetics. The 3% nanocarbon aluminum covetic is also shown to have a 30% higher yield strength as compared to the traditional 0% nanocarbon AA6061 as observed in Figure 33 [49]. Thorough quantificatoin of this mateiral system will be important for future use. Multiscale modeling techniques will be required in order to simulate the nanoscale length effects.

Future work will look at applying the multiscale modeling techniques described in this work with other novel

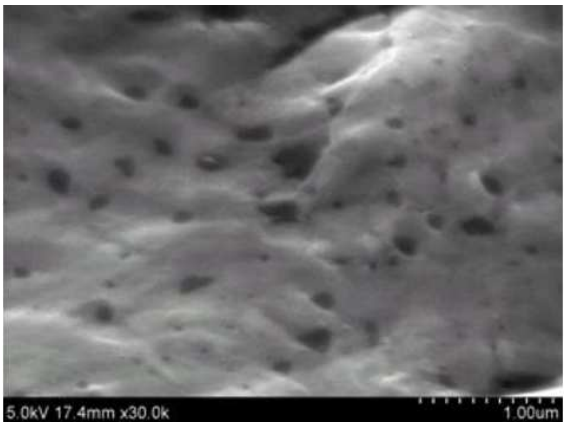

Figure 32: 3 wt.%C AA60601 covetic with nanocarbon particles.

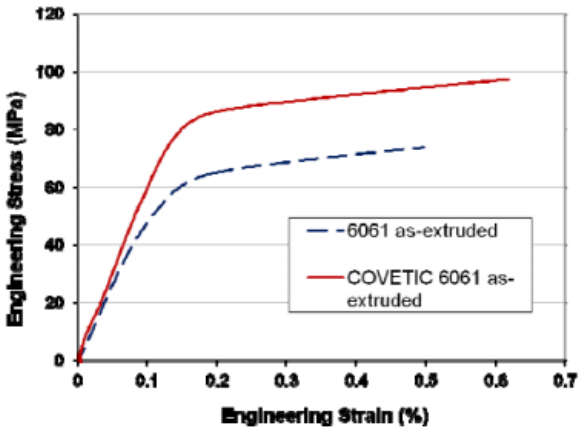

Figure 33: Covetic material yield strength approximately 30 % higher than non-covetic material.

modeling techniques in order to accurately predict the response of this new covetic material system.

References

[1] Grabovac, I. and Whittaker, D., "Applications of bonded composites in the repair of ships structures - A 15-year service experience," *Elseiver Composites: Part A*, 2009.

[2] Bartlett, S. and Jones, B., "Composite Ship Structures," *ASNE Day 2013: Engineering America's Maritime Dominance*, ASNE, Arlington, Virginia, February 21-22 2013.

[3] Chaurasia, A. K. and Seidel, G. D., "Computational micromechanics analysis of electron hopping induced piezoresistive response in carbon nanotube-polymer nanocomposites," *54th AIAA/ASME/ASCE/AHS/ASC Structures, Stuctural Dynamics, and Materials Conference*, Boston, Massachusetts, April 8-11 2013, AIAA 2013-1731.

[4] Saito, R., Dresselhaus, G., and Dresselhaus, M., "Physical Properties of Carbon Nanotubes," *Imperial College Press*, 1998.

[5] Seidel, G. and Lagoudas, D., "Micromechanical analysis of the effective elastic properties of carbon nanotube reinforced composites," *Mechanics of Materials*, Vol. 38, 2006, pp. 884–907.

[6] Schadler, L., Giannaris, S. C., and Ajayan, P. M., "Load transfer in carbon nanotube epoxy composites," *Appiled Physics Letters*, Vol. 73, 1998, pp. 3842–3844.

[7] Xian, R. and Seidel, G. D., "Computational micromechanics modeling of the inherent piezoresistivity in carbon nanotube-polymer nanocomposites," *Journal of Intelligent Material Systems and Structures*, 2013.

[8] Kanda, Y., "Piezoresistance effect of silicon," *Sensors and Actuators*, Vol. 28, 1991, pp. 83–91.

[9] Tombler, T. W., Zhou, C. W., Alexseyev, L., Kong, J., and Dai, H. J., "Reversible electromechanical characteristics of carbon nanotubes under local-probe manipulation," *Nature*, Vol. 405, 2000, pp. 769–772.

[10] Seidel, G. and Lagoudas, D., "A Micromechanics Model for the Electrical Conductivity of Nanotube-Polymer Nanocomposites," *Journal of Composite Materials*, Vol. 43, No. 9, 2009, pp. 917–941.

[11] Park, C., Ounaies, Z., Watson, K., Pawlowski, K., Lowther, S., Connell, J., Siochi, E., Harrison, J., and St. Clair, T., "Polymer-single Wall Carbon Nanotube Composites for Potential Spacecraft Applications," Tech. Rep. NASA/CR-2002-211940, NASA ICASE, 2002.

[12] Ko, F., Khan, S., Ali, A., Gogotsi, Y., Naguib, N., Yang, G., Li, C., Shimoda, H., Zhou, O., Bronikowski, M., Smalley, R., and Willis, P., "Structure and properties of carbon nanotube reinforced nanocomposites," .

[13] Njuguna, J. and Pielichowski, K., "Polymer Nanocomposites for Aerospace Applications: Fabrication," *Advanced Engineering Materials*, Vol. 6, No. 4, 2004, pp. 193–203.

[14] Breuer, O. and Sundararaj, U., "Big Returns From Small Fibers: A Review of Polymer/Carbon Nanotube Composites," *Polymer Composites*, Vol. 25, No. 6, December 2004, pp. 630–645.

[15] Lau, K.-T., Gu, C., and Hui, D., "A critical review on nanotube and nanotube/nanoclay related polymer composite materials," *Composites Part B: Engineering*, Vol. 37, 2006, pp. 425–436.

[16] Kang, I., Schulz, M., Kim, J., Shanov, V., and Shi, D., "A carbon nanotube strain sensor for structural health monitoring," *Smart Materials and Structures*, Vol. 15, 2006, pp. 737–748.

[17] Yakobson, B. and Avouris, P., "Mechanical Properties of Carbon Nanotubes," *Topics in Applied Physics: Carbon Nanotubes*, Vol. 80, 2001, pp. 287–327.

[18] Hone, J., Whitney, M., Piskoti, C., and Zettl, A., "Thermal conductivity of single-walled carbon nanotubes," *Physical Review B*, Vol. 59, No. 4, 1999, pp. R2514–R2516.

[19] Ebbesen, T., Lezec, H., Hiura, H., Bennett, J., Ghaemi, H., and Thio, T., "Electrical conductivity of individual carbon nanotubes," *Nature*, Vol. 382, 1996, pp. 54–56.

[20] Allaoui, A., Bai, S., Cheng, H., and Bai, J., "Mechanical and electrical properties of a MWNT/epoxy composite," *Composites Science and Technology*, Vol. 62, 2002, pp. 1993–1998.

[21] Gojny, F., Wichmann, M., Fiedler, B., Kinloch, I., Bauhofer, W., Windle, A., and Schulte, K., "Evaluation and identification of electrical and thermal conduction mechanisms in carbon nanotube/epoxy composites," *Polymer*, Vol. 47, 2006, pp. 2036–2045.

[22] Potschke, P., Abdel-Goad, M., Alig, I., Dudkin, S., and Lellinger, D., "Rheological and dielectrical characterization of melt mixed polycarbonate-multiwalled carbon nanotube composites," *Polymer*, Vol. 45, 2004, pp. 8863–8870.

[23] Meincke, O., Kaempfer, D., Weickmann, H., Friedrich, C., Vathauer, M., and Warth, H., "Mechanical properties and electrical conductivity of carbon-nanotube filled polyamide-6 and its blends with acrylonitrile/butadiene/styrene," *Polymer*, Vol. 45, 2004, pp. 739–748.

[24] McNally, T., Potschke, P., Halley, P., Murphy, M., Martin, D., Bell, S., Brennan, G., Bein, D., Lemoine, P., and Quinn, J., "Polyethylene multiwalled carbon nanotube composites," *Polymer*, Vol. 46, 2005, pp. 8222–8232.

[25] Hu, G., Zhao, C., Zhang, S., Yang, M., and Wang, Z., "Low percolation thresholds of electrical conductivity and rheology in poly(ethylene terephthalate) through the networks of multi-walled carbon nanotubes," *Polymer*, Vol. 47, 2006, pp. 480–488.

[26] Cooper, C. A., Ravich, D., Lips, D., Mayer, J., and Wagner, H., "Distribution and alignment of carbon nanotubes and nanofibrils in a polymer matrix," *Composites Science and Technology*, Vol. 62, 2002, pp. 1105–1112.

[27] Zhu, J., Peng, H., Rodriguez-Macias, F., Margrave, J., Khabashesku, V., Imam, A., Lozano, K., and Barrera, E., "Reinforcing epoxy polymer composites through covalent integration of functionalized nanotubes," *Advanced Functional Materials*, Vol. 14, No. 7, 2004, pp. 643–648.

[28] Li, X., Gao, H., Scrivens, W., Fei, D., Xu, X., Sutton, M., Reynolds, A., and Myrick, M., "Nanomechanical characterization of single-walled carbon nanotube reinforced epoxy composites," *Nanotechnology*, Vol. 15, 2004, pp. 1416–1423.

[29] Choi, S., Zhang, Z., Yu, W., Lockwood, F., and Grulke, E., "Anomalous thermal conductivity enhancement in nanotube suspensions," *Applied Physics Letters*, Vol. 79, No. 14, 2001, pp. 2252–2254.

[30] Song, Y. and Youn, J., "Influence of dispersion states of carbon nanotubes on physical properties of epoxy nanocomposites," *Carbon*, Vol. 43, 2005, pp. 1378–1385.

[31] Guthy, C., Du, F., Brand, S., Fischer, J., and Winey, K., "Thermal Conductivity of Single-Walled Carbon Nanotube/PMMA Nanocomposites," *Materials Research Society Symposium Proceedings*, Vol. 858E, 2005, HH3.31.1.

[32] Valavala, P. and Odegard, G., "Modeling Techniques for Determination of Mechanical Properties of Polymer Nanocomposites," *Reviews on Advanced Materials Science*, Vol. 9, 2005, pp. 34–44.

[33] Zeng, Q., Yu, A., and Lu, G., "Multiscale modeling and simulation of polymer nanocomposites," *Progress in Polymer Science*, Vol. 33, 2008, pp. 191–269.

[34] Hammerand, D., Seidel, G., and Lagoudas, D., "Computational micromechanics of clustering and interphase effects in carbon nanotube composites," *Mechanics of Advanced Materials and Structures*, Vol. 14, 2007, pp. 277–294.

[35] Seidel, G. and Lagoudas, D., "A Micromechanics Model for the Thermal Conductivity of Nanotube-Polymer Nanocomposites," *Journal of Applied Mechanics*, Vol. 75, 2008, pp. 041025–1–9.

[36] Seidel, G., Lagoudas, D., Frankland, S., and Gates, T., "Micromechanics modeling of functionally graded interphase regions in carbon nanotube-polymer composites," *47th AIAA/ASME/ASCE/AHS/ASC Structures, Stuctural Dynamics, and Materials Conference*, AIAA/ASME/ASCE/AHS/ASC, Newport, Rhode Island, May 1-4 2006, AIAA 2006-1678.

[37] Lagoudas, D. and Seidel, G., "Micromechanics Modeling of the Multi-functional Nature of Carbon Nanotube-Epoxy Nanocomposites: Effective Elastic, Thermal, and Electrical Properties," *6th International Symposium on Advanced Composites*, COMP07, Corfu, Greece, May 16-18 2007, COMP07-021.

[38] Seidel, G., Boehringer, K., and Lagoudas, D., "Analysis of Clustering and Interphase Region Effects on the Electrical Conductivity of Carbon Nanotube-Polymer Nanocomposites via Computational Micromechanics," *Proceedings of the ASME Conference on Smart Materials, Adaptive Structures and Intelligent Systems*, ASME, Ellicott City, Maryland, October 28-30 2008.

[39] Seidel, G. D. and Stephens, S. N., "Analytical and computational micromechanics analysis of the effects of interphase regions and orientation on the effective coefficient of thermal expansion of carbon nanotube-polymer nanocomposites," *51st AIAA/ASME/ASCE/AHS/ASC Structures, Stuctural Dynamics, and Materials Conference*, AIAA/ASME/ASCE/AHS/ASC, Orlando, Florida, April 12-15 2006, AIAA 2010-2809.

[40] Hashin, Z. and Rosen, B., "The elastic moduli of fiber-reinforced materials," *Journal of Applied Mechanics*, Vol. 31, 1964, pp. 223–232.

[41] Yu, M. F., Files, B. S., Arepalli, S., and Ruoff, R., "Tensile loading of ropes of single wall carbon nanotubes and their mechanical properties," *Physical Review Letters*, Vol. 84, 2000, pp. 5552–5555.

[42] Mori, T. and Tanaka, K., "Average stress in matrix and average elastic energy of materials with misfitting inclusions," *Acta Metallurgica*, Vol. 21, 1973, pp. 571–574.

[43] Seidel, G. D., *Micromechanics Modeling of the Multifunctional Nature of Carbon Nanotube-Polymer Nanocomposites*, Ph.D. thesis, Texas A&M University, August 2007.

[44] Lu, P., "Further studies on Mori-Tanaka models for thermal expansion coefficients of composites," *The International Journal for the Science and Tehcnology of Polymers*, Vol. 54, 2013, pp. 1691–1699.

[45] Achenbach, J. and Zhu, H., "Eect of interphases on micro and macromechanical behavior of hexagonal-array ber composites," *ASME Journal of Applied Mechanics*, Vol. 57, 1990, pp. 956–963.

[46] Dvorak, G. and Teply, J., "Plasticity Today: Modeling, Methods and Applications," *Elsevier*, 1985.

[47] Fisher, F. T., "Nanomechanics and the viscoelastic behavior of carbon nanotube-reinforced polymers," 2002.

[48] Cooper, C. A., Ravich, D., Lips, D., Mayer, J., and Wagner, H., "Distribution and alignment of carbon nanotubes and nanobrils in a polymer matrix," *Composites Science and Technology*, Vol. 62, 2002, pp. 1105–1112.

[49] *Novel Metal-Matrix Composites with Inegrally-Bound Nanoscale Carbon*, Nanotech Conference and Expo 2012, June 2012.